IOP Publishing Plasma Sources Science and Technology
Plasma Sources Sci. Technol. **30** (2021) 065002 (18pp) https://doi.org/10.1088/1361-6595/abe612

Modeling of fast ionization waves in pure nitrogen at moderate pressure

Xiancong Chen[1], Yifei Zhu[1,2,*], Yun Wu[1,2], Jinbo Hao[3], Xiaoguang Ma[4] and Pengfei Lu[3,5]

[1] Science and Technology of Plasma Dynamics Laboratory, Airforce Engineering University, Xi'an 710038, Shaanxi, People's Republic of China
[2] Institute of Aero-engine, School of Mechanical Engineering, Xi'an Jiaotong University, Xi'an 710049, Shaanxi, People's Republic of China
[3] School of Science, Xi'an University of Architecture and Technology, Xi'an 710055, Shaanxi, People's Republic of China
[4] School of Physics and Optoelectronic Engineering, Ludong University, Yantai 264025, Shandong, People's Republic of China
[5] State Key Laboratory of Information Photonics and Optical Communications, Beijing University of Posts and Telecommunications, Beijing 100876, People's Republic of China

E-mail: yifei.zhu.plasma@gmail.com

Received 27 November 2020, revised 30 January 2021
Accepted for publication 12 February 2021
Published 2 June 2021

Abstract

The fast ionization wave (FIW) discharges in pure nitrogen in a capillary tube at 27 mbar, initiated by positive polarity, high-voltage nanosecond pulses, are numerically studied by coupled two-dimensional plasma fluid modeling. The 2D fluid code based on local mean energy approximation is validated and used, an extended three-exponential Helmholtz photoionization model is proposed for pure nitrogen. The development and structure of the nitrogen FIW is analyzed, the electric field and current are calculated compared with experimental measurements. The evolution of radial distribution of electrons and $N_2(C^3\Pi_u)$ during the FIW development stage and in the afterglow are analyzed, the radial profiles of electron density show a 'hollow' structure in the FIW development stage, the temporal-spatial evolution of $N_2(C^3\Pi_u)$ is dominated by the competition between the pooling reaction of $N_2(A^3\Sigma_u^+)$ and the quenching by electrons. The role of photoionization on the nitrogen FIW radial morphology is discussed, the equivalent background electron density of photoionization in nitrogen discharge is suggested to be (4–6) $\times 10^{13}$ m^{-3}. Spatial distribution of specific energy deposition (SED), fast gas heating (FGH) energy and temperature rise are obtained, heating efficiency varies with electric field E/N and SED and tends to be 10% at high SED. The dominating reactions responsible for FGH and their fractional contribution in space and time are analyzed, in the near axis region, pooling reactions of $N_2(A^3\Sigma_u^+)$ and $N_2(B^3\Pi_g)$ contribute up to 80% FGH energy, electron impact dissociation of molecular nitrogen contributes about 10%, while e-N_2^+ recombination and quenching of $N(^2D)$ atoms by N_2 molecules contribute rest.

Keywords: fast ionization wave, nanosecond pulsed discharge, nitrogen plasma, plasma fluid modeling

(Some figures may appear in colour only in the online journal)

* Author to whom any correspondence should be addressed.

1. Introduction

In the last two decades, plasmas produced by nanosecond pulsed discharges have been widely utilized and studied in various fields, e.g. flow control [1–3], ignition/combustion [4–7], energy transition, fuel reforming [8–11] and biological medicine [12, 13]. High voltage pulses (positive or negative polarity) with a rapid rising slope ($O(1)$ ns) and short pulse width ($O(10)$ ns) can produce strong non-equilibrium plasmas usually in the form of a guided streamer [14], due to the strong electric fields ($\sim 10^3$ Td) in the fronts of nanosecond discharges and high chemical activity in the afterglow.

To study the properties of the plasma kinetics in nanosecond pulsed discharges, good reproducibility of discharge parameters and spatial uniformity are preferred. To achieve such conditions, fast ionization wave (FIW) discharge operating at moderate pressures (usually below 100 mbar) and moderate repetitive frequency ($O(10)$ Hz) is proposed and studied [15–17]. The FIW is characterized with good reproducibility of discharge parameters and spatial homogeneity of plasmas, high electric fields and high-energy electrons, high propagation velocity (10^9–10^{10} cm s^{-1}), and high excitation/dissociation degrees ($>1\%$) and thus high chemical reactivity.

FIWs produced by nanosecond capillary discharges (nCD) at moderate pressures have stimulated intensive interests of the plasma community. Two-photon absorption laser-induced fluorescence (TALIF) technique was used to measure the O-atom density on a microsecond time scale, in a capillary nanosecond discharge initiated in air at 24–30 mbar, with about 1 eV molecule^{-1} specific energy deposition (SED) [18, 19]. A high dissociation degree ($>50\%$) of molecular oxygen after 2 μs was achieved, the high dissociation efficiency can be attributed to the collisional dissociation of oxygen with electronically excited nitrogen molecules e.g. $N_2(A^3\Sigma_u^+)$, $N_2(B^3\Pi_g)$, $N_2(C^3\Pi_u)$ and $N_2(a'^1\Sigma_u^-)$ [20, 21]. A similar experiment conducted by the same group [22] recently achieved a 9.7% dissociation degree in pure nitrogen with SED of the 1.67 eV molecule^{-1}, stepwise dissociation of electronically excited molecules $N_2(A^3\Sigma_u^+)$, $N_2(B^3\Pi_g)$, $N_2(C^3\Pi_u)$ by electron impact, was proposed to explain the high dissociation degree. In addition, new chemical mechanisms discovered through the iteration between experiments and 1D kinetics modeling, e.g. the fast quenching of $N_2(C^3\Pi_u)$ by electrons [23], pooling reaction of $N_2(B^3\Pi_g)$ accounting for fast gas heating (FGH) in nitrogen plasma [24] was proposed to explain some particular characteristics of plasmas at high SED.

Electric field induced second harmonic (E-FISH) generation, a recently developed laser-based diagnostic with excellent temporal (sub-nanosecond) and spatial (sub-millimeter) resolution [25–27], was used to resolve FIW dynamics recently. The E-FISH diagnostic of the electric field in FIW discharges in nitrogen at 20–100 mbar can be found in reference [28], the high temporal resolution of such measurements indicated a possibility of detection of non-local electron kinetics effects induced by a rapidly varying, high peak value electric field in low and moderate pressure FIW discharges. Furthermore, E-FISH combined with TALIF, was performed by Chng *et al* [29] to understand the impact of the electric field on atomic species production in pure nitrogen FIW discharge in a 2 cm diameter tube at 20 mbar. A relatively low peak N-atom density of about 5.5×10^{12} cm^{-3} was obtained at low SED (about 0.01 eV molecule^{-1}). Attempts via 1D kinetics modeling showed that simulation results were strongly influenced by the radial non-uniformity of the discharge.

Numerical modeling of FIW via global chemistry code, 1D model based on radial approximation (aforementioned [21–24])/axial simplification or the self-consistent 2D model have been conducted. The optical actinometry method together with 0D modeling [30] is proposed to obtain the absolute O-atom densities in the early afterglow of FIW at high SED. Takashima *et al* [17] analyzed the FIW propagation in nitrogen and helium using quasi-1D model and 2D fluid model via *nonPDPSIM* [31, 32]. Similar studies [33, 34] revealed the effect of pulse repetition rate on FIW in helium/argon/neon at different pressures via 1D modeling and experiments. Impressive 2D modeling on FIW via hybrid code *nonPDPSIM* in air at 27 mbar can be found in [35], where the calculated FIW propagation velocity, current rise and E/N rise agreed well with experiments. A cycle of 2D numerical studies on FIWs in flexible capillary tubes were conducted by Xiong *et al* [36–38], the propagation mechanisms of FIWs in Ne/Xe gas mixture at atmospheric pressure and possible influencing factors were analyzed. Reference [39] numerically studied the streamer and FIW mode of nCD in air in a short tube (2 cm), the influence of SED on the temporal-spatial evolution of e and $N_2(C^3\Pi_u)$ was discussed for the flexible control of kinetics.

Despite the aforementioned progress, there are few works devoting to fully coupled multidimensional self-consistent modeling (coupling discharge and fluid) of FIW discharge/afterglow in pure nitrogen. The difficulties come from the computational cost, the simulation of the conductive stage, the treatment of the photoionization source and floating electrode. The aim of this work, is to model FIW in pure nitrogen in a full dimension long tube (7 cm) by a coupled code to obtain information for detailed kinetics analysis. The simulation conditions (i.e. geometry of the discharge setup, applied voltage etc.) are kept exactly the same with the experiments [23], the calculated results are compared with measurements. Several issues that experimentalists are interested in, e.g. inception, development, species evolution and FGH are discussed.

A description of the model and the implementation of experimental conditions is given in section 2, code validation is presented in section 3. The problems involved with the inception, propagation and afterglow of FIW are discussed in section 4, as well as energy properties including FGH. The conclusions are given in section 5.

2. Model description and experimental implementation

The 2D PASSKEy (PArallel Streamer Solver with KinEtics) code is used. The code has been used in the modeling of nanosecond surface discharges [40–43] and validated by measured discharge morphology, propagation velocity, voltage–current curves of experiments, a pin-to-plane model

benchmark [44] and discharges concerning streamer-to-spark transitions [45]. Detailed mathematical formulations, the strategy for multiphysics and multiscale coupling, and validations can be found in paper [40, 42]. Here we briefly presented the equations solved, and introduce the key implementations that are necessary for modeling nitrogen FIW.

2.1. Fluid model formulation

The classical fluid model is used for discharge dynamics, drift-diffusion–reaction equations for species, the electron energy equation for mean electron energy, Poisson's equation for electric field, Helmholtz equations for photoionization and Euler equations for fluid dynamics are fully coupled. The plasma fluid equations are written as follows:

$$\frac{\partial n_i}{\partial t} + \nabla \cdot \mathbf{\Gamma_i} = S_i + S_{\rm ph}, \quad i = 1, 2, \ldots, N_{\rm total} \tag{1}$$

$$\mathbf{\Gamma_i} = (q_i/|q_i|)\mu_i n_i \boldsymbol{E} - D_i \nabla n_i, \quad i = 1, 2, \ldots, N_{\rm ch} \tag{2}$$

$$\frac{\partial}{\partial t}(n_{\rm e}\epsilon_{\rm m}) + \nabla \cdot \mathbf{\Gamma_\epsilon} = -|q_{\rm e}| \cdot \mathbf{\Gamma}_{\rm e} \cdot \boldsymbol{E} - P(\epsilon_{\rm m}) \tag{3}$$

$$\mathbf{\Gamma_\epsilon} = -n_{\rm e}\epsilon_{\rm m}\mu_\epsilon \boldsymbol{E} - D_\epsilon \nabla(n_{\rm e}\epsilon_{\rm m}) \tag{4}$$

$$\nabla(\varepsilon_0 \varepsilon_r \nabla\Phi) = -\rho - \rho_{\rm c} \tag{5}$$

$$\boldsymbol{E} = -\nabla\Phi, \rho = \sum_{i=1}^{N_{\rm ch}} q_i n_i \tag{6}$$

$$\frac{\partial \rho_{\rm c}}{\partial t} = \sum_{j=1}^{N_{\rm ch}} q_j[-\nabla \cdot \mathbf{\Gamma_j}], \tag{7}$$

where n_i, q_i, $\mathbf{\Gamma_i}$, μ_i and D_i are the number density, charge, flux, mobility and diffusion coefficients for each species i, respectively. The source function S_i includes production and loss terms due to gas phase reactions and is calculated with detailed kinetic processes (kinetics scheme see appendix A), $S_{\rm ph}$ is the photoionization source terms for e, N_2^+ and are calculated via three-exponential Helmholtz equations [46, 47], details will be discussed in section 2.2. $\epsilon_{\rm m}$ is the mean electron energy, μ_i and D_i for electron and electron energy and the rate coefficients of electron impact reactions are represented as explicit functions of $\epsilon_{\rm m}$ based on LMEA [48]. The diffusion coefficient and mobility for ions are extracted from experimental data [49]. In the code, $\nabla \cdot \mathbf{\Gamma_i} = 0$ for neutral species is postulated. $P(\epsilon_{\rm m})$ represents the power lost by electrons in collisions ($P(\epsilon_{\rm m}) = P_{\rm loss}/N_{\rm g} \times N_{\rm g} \times n_{\rm e}$, $N_{\rm g}$ the gas density) and $P_{\rm loss}/N_{\rm g}$ is obtained from BOLSIG+ [48]. Φ is the electric potential, $\boldsymbol{E}$ the electric field, ε_0 is the vacuum permittivity, $\varepsilon_{\rm r}$ the relative permittivity, $\rho_{\rm c}$ the dielectric surface charge density. $N_{\rm total}$ and $N_{\rm ch}$ are the number of all species and charged species, respectively.

LMEA is used in this work, due to the large sheath region near the dielectric at moderate pressures: as the streamer is coming closer to the solid surfaces (i.e. cathode or dielectric surfaces) the strong gradient of the electron density is created (sheath region). The strong gradient of density result in the strong diffusion flux of electrons against the electric force (diffusion flux is larger than convection flux), thus electrons are losing their energy ($-\mathbf{\Gamma}_{\rm e} \cdot \boldsymbol{E} < 0$ in equation (3), so-called 'electron energy cooling by field'), being unable to produce strong ionization. Reference [41] have analyzed the application conditions of LFA and LMEA and have mentioned that LMEA is preferred for the modeling of capillary discharges in low pressures.

A set of Euler equations are solved for gas temperature and density variations. The coupling strategy between plasma equations and Euler equations have been described in detail in reference [42].

2.2. Extended three-exponential Helmholtz photoionization model

The three-exponential Helmholtz model was proposed to calculate the photoionization source term of $N_2 : O_2$ mixtures [46, 47], a table of fitting coefficients are provided based on the measured photoionization functions.

However, the classical three-exponential Helmholtz model assumes that photoelectrons come from the ionization of O_2 molecules by VUV-radiation of N_2 in $b^1\Pi_u$, $b'^1\Sigma_u^+$, $c'^1_4\Sigma_u^+$ states [50], thus the model and corresponding parameters are valid only for $N_2 : O_2$ mixtures.

In pure nitrogen, the radiation with wavelengths below 79.5 nm (corresponding to the ionization potential of nitrogen 15.6 eV) is produced by the dissociation ionization of N_2 molecules and subsequent $N_{\rm II}$ ($\lambda < 80$ nm) transition [51]:

$$N_2 + e \rightarrow N^+(^1P^0, {}^3P^0) + N + 2e \tag{8}$$

$$N^+(^1P^0, {}^3P^0) \rightarrow N^+(^3P) + 67.1\ \text{nm}. \tag{9}$$

To calculate the photoionization source term for pure nitrogen discharge, we extended the classical three-exponential Helmholtz model into a more general form by replacing the partial pressure of oxygen molecules p_{O_2} with total pressure p:

$$S_{\rm ph}(\vec{r}) = \sum_j S_{\rm ph}^j(\vec{r}) \tag{10}$$

$$\nabla^2 S_{\rm ph}^j(\vec{r}) - (\lambda_j p)^2 S_{\rm ph}^j(\vec{r}) = -A_j p^2 \frac{p_q}{p + p_q} I(\vec{r}) \tag{11}$$

$$\frac{\Psi_0(r)}{p} = (pr)\sum_j A_j {\rm e}^{-\lambda_j pr} \tag{12}$$

$$\frac{\Psi_0(r)}{p} = \frac{1}{4\pi}\frac{\omega}{\alpha_{\rm eff}} \frac{\int_{\lambda_{\rm min}}^{\lambda_{\rm max}} \xi_\lambda(\mu_\lambda/p)\exp((-\mu_\lambda/p)pr) I_\lambda^0 {\rm d}\lambda}{\int_{\lambda_{\rm min}}^{\lambda_{\rm max}} I_\lambda^0 {\rm d}\lambda}, \tag{13}$$

where λ_j and A_j ($j = 1, 2, 3$) are fitting parameters for equation (12). I is the ionization source rate, $p_q = 9.8$ Torr is the quenching pressure of emitting species. $\Psi_0(r)/p$ the photoionization functions as pr obtained via experimental measurements at low pressures and are presented in [51], ω the excitation coefficient of emitting states, $\alpha_{\rm eff}$ the effective Townsend coefficient, ($\lambda_{\rm min}$, $\lambda_{\rm max}$) the spectral range of radiation, ξ_λ and μ_λ are the spectrally resolved photoionization yield and absorption coefficient, respectively, I_λ^0 is the spectral density of ionizing radiation.

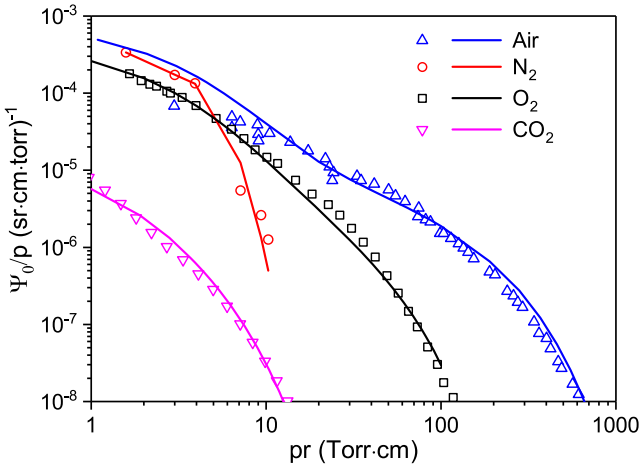

Figure 1. Photoionization functions Ψ_0/p of air, O_2, N_2, CO_2. The hollow symbols and solid lines represent experimental values extracted from reference [51] and calculated values by the PHOTOPiC package, respectively. Reused data from [51]. © IOP Publishing Ltd. All rights reserved.

Table 1. Parameters of the three-exponential fit of $\Psi_0(r)/p$ as a function of pr.

j	A_j (cm^{-2} Torr^{-2})	λ_j (cm^{-1} Torr^{-1})
1	0.066 46	1.3121
2	1.3580	1.5238
3	−1.4165	1.5097

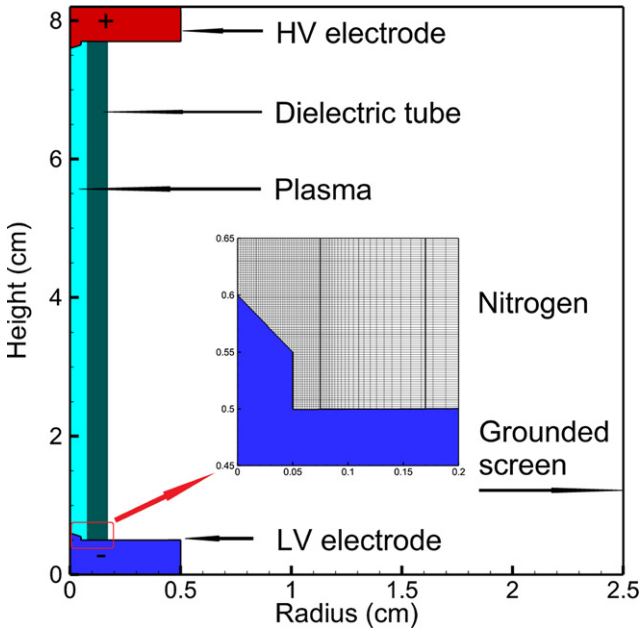

Figure 2. 2D cylindrical geometry for FIW discharge with an enlargement of low-voltage electrode showing the mesh refinement. The internal and external diameter of the tube is 1.5 mm and 3.4 mm, respectively, the inter-electrode gap is 70 mm. The diameter of the cylindrical parts of the electrodes inside the tube is equal to 1 mm and the radius of tips of the electrodes is about 0.1 mm. The central position of the capillary tube is defined at $r = 0$, $z = 4.1$ cm.

With the extended three-exponential Helmholtz model, the partial pressure of specific gas is no longer needed, it is possible to calculate photoionization source term of pure/multi-species (any ratio) gas discharges if a valid photoionization function is available for parameters fitting.

The photoionization function can be obtained by direct measurements or by calculation [51]. A free online toolbox PHOTOPiC is developed and used for this aim. Using the product of spectrum emission intensity, the photoionization yield and the absorption coefficients as the input to PHOTOPiC, the photoionization functions Ψ_0/p of air, O_2, N_2, CO_2 is well reproduced, see figure 1.

Note that the fitting for N_2 is effective only when $pr \leqslant 10$ Torr cm due to the upper limit of three-exponential fit, it means the photoionization within $r \leqslant 10/20.25 \approx 0.5$ cm (27 mbar = 20.25 Torr) can be effectively modeled. According to reference [52], the size of the region in which we need to consider photoionization depends on the streamer head size and the absorption length of photoionization radiation, and can be estimated as 1/2 the radius of the streamer head. In this work, the radius of the streamer head is limited by capillary tube, $R = 0.75$ mm $\ll 0.5$ cm. Therefore, this three-exponential model is capable of resolving the photoionization at 27 mbar.

The six parameters required in the extended three-exponential Helmholtz model are then obtained by fitting the photoionization function using the Nelder–Mead simplex direct search method, see table 1.

2.3. Implementation of experimental conditions

Details of the experiments can be found in references [23, 24, 30]. The discharge was initiated in a capillary quartz tube with an internal diameter of 1.5 mm and an external diameter of 3.4 mm, and an inter-electrode gap of 70 mm. The capillary is filled with pure nitrogen at 27 mbar and 300 K, the influence of gas flow on gas density is negligible. Two grounded aluminum plates enclose the capillary from above and below. Adhesive aluminum sheets complete this construction to form a closed, grounded screen having a rectangular cross section. The discharge tube is terminated by two metal pin-shaped high (HV) and low (LV) voltage electrodes. The HV electrode is connected to an HV generator that supplies the voltage pulses. The LV electrode is left unterminated and connected to the long cable. The sequence of pulses applied to the discharge tube consisted of three main pulses separated by 245 ns; only the first main pulse is studied in this work.

The simplified cylindrical geometry for the calculation is presented in figure 2. The geometry consists of a quartz capillary tube with relative permittivity $\varepsilon_r = 4$. The computational domain is 2.5 cm × 8.2 cm, with a uniform 20 μm mesh refinement in the plasma region, the total number of grid cells is about 320 000, of which about 135 000 are distributed in plasma region.

Boundary conditions for transport equations is assigned according to species and materials. At the anode (HV), the positive ions flux are fixed as zero while the electron flux is estimated using homogeneous Neumann conditions. At the cathode (LV), the homogeneous Neumann conditions are

applied for all charged species flux. At the plasma-dielectric interface, all charged species flux towards to the surface is estimated using homogeneous Neumann conditions, while all positive species flux outwards to the surface is fixed as zero. Electron flux outward to the dielectric is due to secondary electron emission by ion bombardment, $\Gamma_e = -\gamma\Gamma_{ion}$, $\gamma = 0.01$ in this work, our test shows the value of γ ranging from 0.005 to 0.3 have negligible influence on discharge propagation parameters. Surface photoemission is not considered in this work, as during our previous trials modeling nCD [39], the photoemission was not found to affect the propagation of the discharge in conditions of this work.

For electron energy equation, the flux at plasma-material interfaces keep consistent with electron transport equation. At boundaries where electrons are transported from plasma to the surface $\Gamma_\epsilon = \Gamma_e \times \epsilon_m$ (ϵ_m is the electron energy of the last plasma cell in eV); at boundaries where electron are emitted from surface $\Gamma_\epsilon = \Gamma_e \times 0.01$ eV.

For Poisson's equation, the Dirichlet boundary condition $\Phi = \Phi(t)$ is applied for HV and LV. The voltage applied to HV is a pulse with 9.3 kV in amplitude, 4 ns rise time and 29 ns FWHM, see figure 5(a), the summation of the incident and reflected voltages is used as the potential of HV ($\Phi = U_{inc}(t) + U_{reflec}(t)$). The LV is treated as floating electrode with the potential $\Phi_{LV} = IZ$ (the value is equal to transmitted voltage), where I is the conductive current at the LV surface, $Z = 50\,\Omega$ is the wave resistance of the cable [23].

The initial electron density is $n_{e0} = 10^{10}$ m^{-3} uniformly distributed in the capillary tube, the ion density is given based on quasi-neutrality. The initial electron density is defined based on two facts: (i) physically, the repetitive frequency of HV pulse is 10 Hz in experiment [23], the time gap between two pulses is enough for plasmas to decay to a sufficiently value—background ionization density ranging 10^9–10^{10} m^{-3} due to cosmic radiation [53]; (ii) numerically, we varied this initial density by one order of magnitude and we found this low value has negligible influence on discharge parameters, because the electrons provided by photoionization exceed this value far beyond. The initial mean electron energy is set as $\epsilon_m = 0.01$ eV. The initial charge density on both space and surfaces is zero.

3. Benchmarks

Two classical cases are considered in this work as benchmarks for comparison: (i) the numerical study [54] of the discharge propagation in a capillary tube in atmospheric air and (ii) an experimental investigation [35] of nanosecond capillary discharge in 27 mbar air.

Case 1: *capillary discharge in atmospheric pressure air*. The discharge is initiated by a pin-to-plane configuration in a $\phi = 100$ μm capillary tube, with a grounded plane electrode and a metallic pin-connected plane holder from below and above enclosing the tube. The pin-plane distance is 5 mm, the tip of the pin is a semi-sphere with a curvature radius of 25 μm, the internal and external radius of the tube is 100 μm and 1100 μm respectively, and the relative permittivity of the dielectric is 5. Constant 6 kV voltage is applied to the pin. The computational domain is 1 cm $\times$ 1 cm in PASSKEy, with a uniform 2.5 μm mesh refinement in region 100 μm $\times$ 0.6 cm.

The comparison with benchmark results are presented in figure 3(a). Note that in [54], the fluid model is based on LFA. Despite this difference, the results calculated by PASSKEy code still shows good agreement in streamer propagation velocity, electron density, electric field and discharge morphology.

Case 2: *nanosecond capillary discharge in moderate pressure air*. The geometry of discharge setup is same as described in section 2.3, but the inter-electrode gap is 8 cm. The capillary tube is filled with synthetic air ($N_2 : O_2 = 4 : 1$) at 27 mbar and 300 K, the voltage applied to HV electrode is a pulse with 9.8 kV in amplitude, 4 ns rise time and 29 ns FWHM. Numerical model, initial/boundary conditions used to reproduce this benchmark is same as described in sections 2.1 and 2.3. Experimental measurements [35] and calculated axial electrical potential profiles at $t = 1$–9 ns are shown in figure 3(b). In the experiments, the electrical potential was measured by moving a capacitive probe along a line parallel to the capillary axis at $r = 12.7$ mm. The potential profiles obtained from calculations agree well with the experimental measurements. The speed of FIW was determined from the peak electric field deduced from the difference of potential profiles along the axial direction. Both calculations and experiments provide an FIW speed ≈ 1.4 cm ns^{-1}.

Additional validations can be found in the following section, by comparing the simulation with the measured field and current value.

4. Results and discussion

In this section we present the features of nitrogen FIW: the electrical properties, the inception, propagation and energy characteristics in the plasma channel.

4.1. Propagation and electrical properties

The electron density and electric field E/N during the FIW propagation stage are shown in figure 4. The FIW has an average propagation speed of 0.7 cm ns^{-1} in nitrogen. The electron density increases to (1–3) $\times$ 10^{20} m^{-3} in the head of the ionization wave during its propagation across the inter-electrode gap, with the higher electron density and E/N near the dielectric wall. E/N in the head of the ionization wave exceeds 10 000 Td, the value is consistent with recent 2D modeling on air FIW at 28.5 mbar [35, 39], the high E/N produces an ionization rate of (1–3) $\times$ 10^{30} m^{-3} s^{-1}.

Once the inter-electrode gap is closed by FIW after 14 ns, the tube is filled with the quasi-uniform plasma with the electron density exceeding 5×10^{20} m^{-3} and quasi-uniform E/N with a relatively low value (hundreds of Td). In fact, the uniform electron density and E/N are not formed instantaneously when the head of the ionization wave touches the LV electrode, the rebound of ionization wave (so-called return stroke) is formed due to the impedance mismatching between the conductive ionized channel [55], the time scale of this process is much shorter than that of the primary ionization wave. A

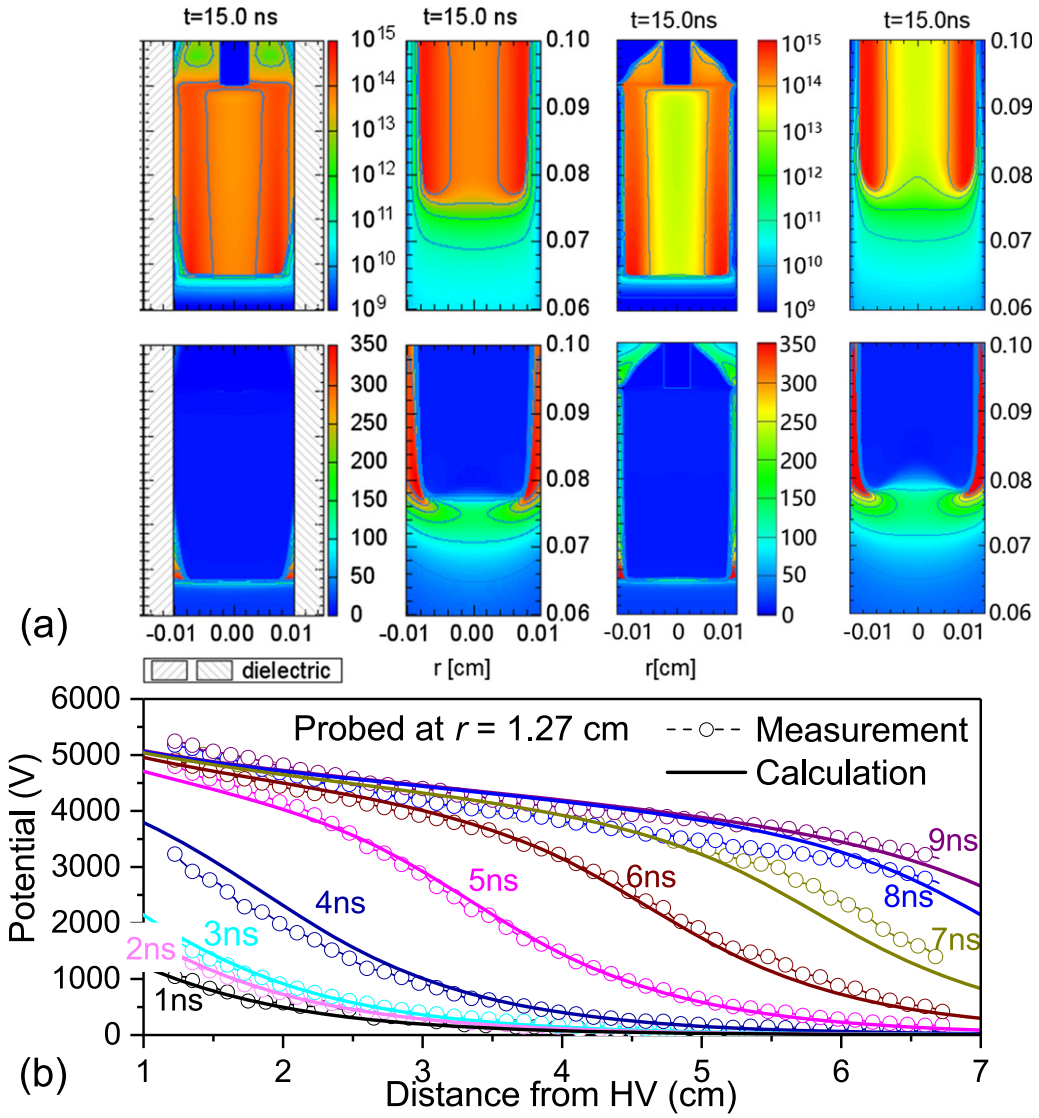

Figure 3. Two benchmark cases for the PASSKEy code. (a) The benchmark case describing the capillary discharge in atmospheric air, reproduced from [54]. © IOP Publishing Ltd. All rights reserved. Contours of electron density and electric field, and corresponding enlargement at time moment 15 ns. The left side is benchmark results, the right side is calculated results. (b) Comparison of axial potential profiles obtained from capacitive probe measurement and the calculation at time moments $t = 1$–9 ns, $r = 12.7$ mm. Reproduced from [35]. © IOP Publishing Ltd. All rights reserved.

sheath with the electron density lower than 10^{19} m^{-3}, and high E/N (nearly 20 000 Td), is formed near the dielectric wall, having a thickness of about 250 μm. The voltage drop across the sheath is about 2000 V and the sheath thickness corresponds to about $20\lambda_D$ (λ_D the Debye length).

The calculated transmitted voltage pulse is plotted together with the measured incident, reflected and transmitted voltage waveforms extracted from [23] in figure 5. Temporal profiles of calculated and measured electric fields and currents are shown in figure 5(b). Quantitative agreement between the measured and calculated results are achieved: the calculated field copies the measurement in the peak and afterglow. Note that calculated peak E/N (14 000 Td) is much higher than the measured one due to higher temporal resolution in the simulation.

During the quasi-steady-state discharge stage ($t > 15$ ns), the electric field in the ionized channel is rather uniform, and can be calculated by the formula ('uniform field' line, see figure 5(b)):

$$E = \frac{U_{\rm inc}(t) + U_{\rm reflec}(t) - U_{\rm trans}(t)}{L}, \qquad (14)$$

where $U_{\rm inc}(t)$, $U_{\rm reflec}(t)$ and $U_{\rm trans}(t)$ represents the incident, reflected and transmitted voltages, $L = 70$ mm is the inter-electrode distance.

Despite the similarities, we notice that, during 0–6 ns and 9–13 ns period, the calculation and measurements significantly differ:

(a) The 0–6 ns period: The measured electric field is rather high (150 Td) before the head of the ionization wave reaching the observation point, like a 'shoulder', however it was not reproduced in the calculation. We compared the Laplacian field of the observation point and at the experimental probing point, E/N at both two positions show

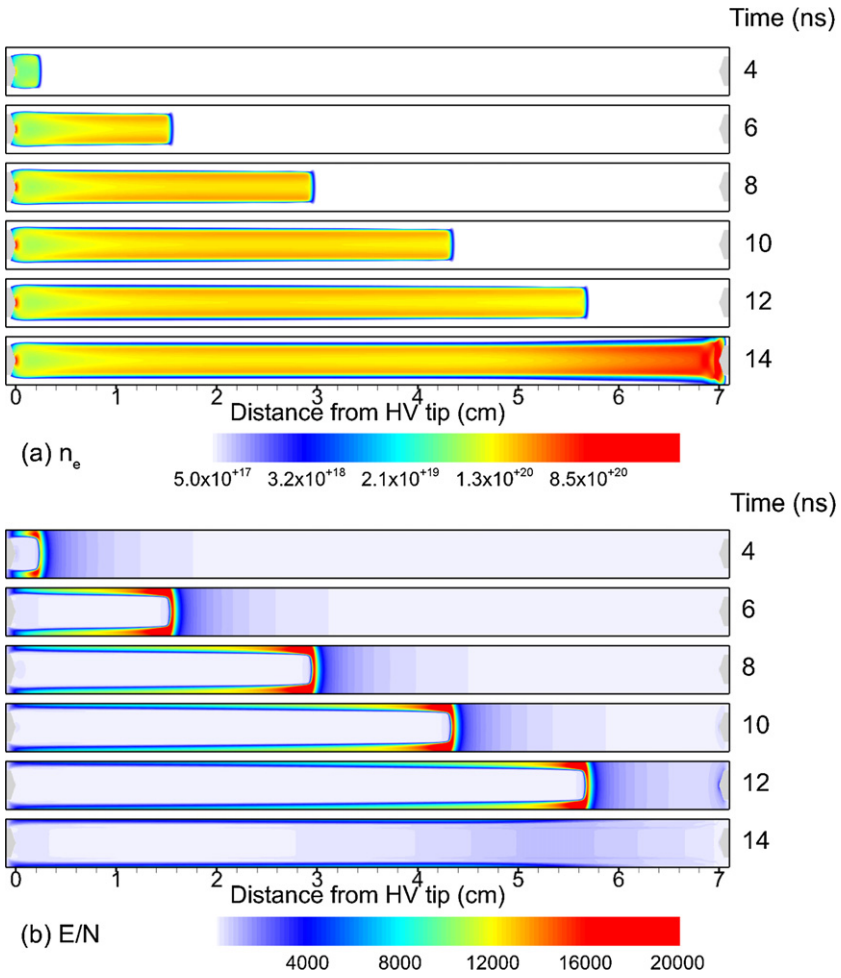

Figure 4. Propagation dynamics of FIW in the capillary tube. (a) Electron density n_e in unit of m^{-3}; (b) electric field E/N in Td (10^{-21} V m^2). The tube radius is 0.75 mm.

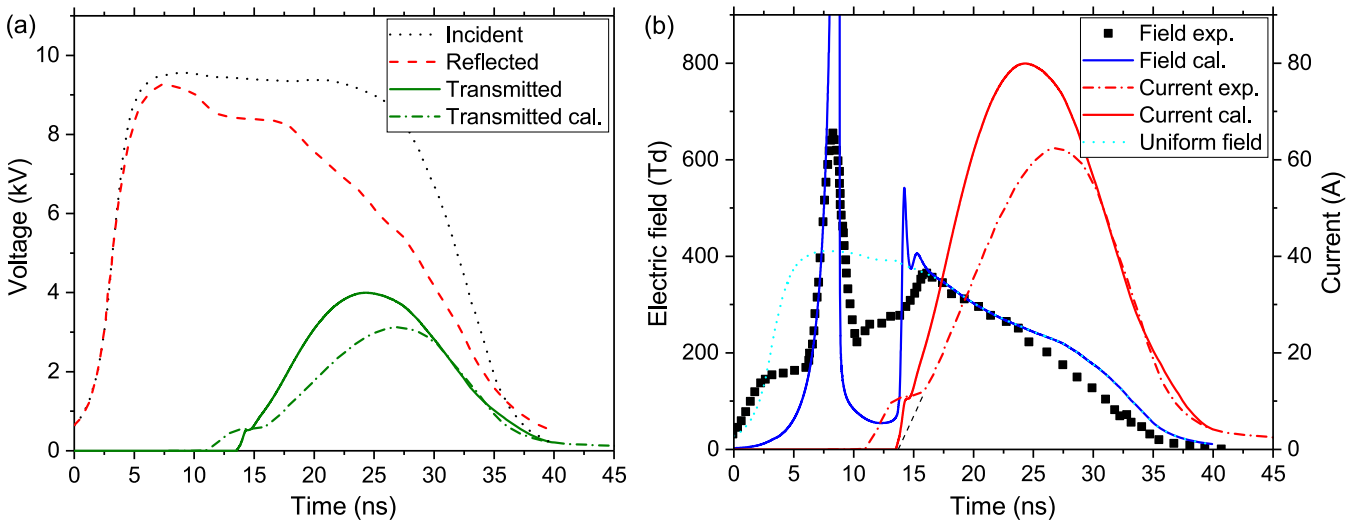

Figure 5. Measured and calculated electric parameters in FIW discharge. (a) Measured incident, reflected and transmitted voltage waveforms (reused data from [23]. © IOP Publishing Ltd. All rights reserved, the original time axis of [23] is move 5 ns to the right to coincide with the moment of beginning to calculate in this work), and calculated transmitted voltage, see explanation in the text; (b) measured and calculated electric field E/N and current, and the uniform field (calculated by equation (14)). The observation point of E/N is the center of inter-electrode gap, $r = 0$, $z = 4.1$ cm. E/N is measured by custom-made calibrated capacitive probe, the current is measured by back current shunts.

the same trend and no 'shoulder' is seen. We then compared the measured field and uniform field calculated by equation (14) in figure 5(b), their values are very close to each other in the first 2.5 ns, however we have no evidence showing that at this moment the tube has already been filled with conductive plasma. In fact, the 'shoulder' of E/N appears not only in the FIW discharge at moderate pressures, but also in the overvoltage pin-to-plane discharges [56] in atmospheric air. More discussions on the 'shoulder' issue will be explained in the future papers.

(b) The 9–13 ns period: after the head of ionization wave passes the observation point and before reaching the end, the calculated E/N is 2–3 times lower than the measurement. The comparison of CP with E-FISH (0.2 ns temporal resolution) indicates that the accuracy of CP in this region drops down [28], measurements with more accurate methods are required.

4.2. Radial distribution of electrons and $N_2(C^3\Pi_u)$

Radial distribution of electrons and the emitting species $N_2(C^3\Pi_u)$ are of interest for the kinetics modeling group to define the initial conditions and for the experimenters to compare with and adjust the optical measurements. The radial-temporal evolution of these two species in nitrogen FIW are presented and discussed.

In the propagation stage, electron density has its maximum off the symmetric axis of the capillary tube at $r = 0.36$ mm (curve 1 in figure 6(a)), in good agreement with reference [23]. In the afterglow, radial electron density changes slowly at a relatively high level ($\sim 10^{20}$ m^{-3}) in the entire first pulse, which is also in good agreement with previous 2D/1D modeling studies on the long-lived plasma characteristics [23] of FIW discharges.

The radial distribution of electrons can be explained by the balance between three pathways: electron impact ionization, e-N_2^+ recombination and associative ionization. The corresponding governing equations can be written as follows:

$$\frac{\mathrm{d}n_\mathrm{e}}{\mathrm{d}t} = k_\mathrm{i}(\varepsilon_\mathrm{m})n_\mathrm{e}[\mathrm{N_2}] - k_\mathrm{rec}n_\mathrm{e}[\mathrm{N_2^+}] + \sum_j k_\mathrm{as}^j[\mathrm{N_2^*}][\mathrm{N_2^{**}}], \quad (15)$$

where $k_\mathrm{i}(\varepsilon_\mathrm{m})$, k_rec and k_as^j is the rate constant of the ionization of grounded N_2 by electron impact, that of electron–ion recombination and that of associative ionization respectively, $[\mathrm{N_2^*}]$ and $[\mathrm{N_2^{**}}]$ are excited states of N_2 involved with the associative ionization ($N_2(A^3\Sigma_u^+, v \leqslant 2)$, $N_2(A^3\Sigma_u^+, v > 2)$ and $N_2(a'^1\Sigma_u^-)$). Here we neglect the source terms from reactions concerning N-atoms and N_4^+ due to their low reaction rates. When $t > 30$ ns, the ionization rate can be neglected, assuming $T_\mathrm{e} = 0.5$ eV and we have $n_\mathrm{e} \sim 10^{20}$–$10^{21}$ m^{-3}, the electron–ion recombination rate can be estimated as $k_\mathrm{rec}n_\mathrm{e}[\mathrm{N_2^+}] \sim 10^{28}$–$10^{29}$ m^{-3} s^{-1}, while the rate of associative ionization $\sum_j k_\mathrm{as}^j[\mathrm{N_2^*}][\mathrm{N_2^{**}}] \sim 6 \times 10^{27} - 3 \times 10^{28}$ m^{-3} s^{-1}, the rates for production and loss are in the same order of the magnitude, the long-lived plasma is maintained by high density of the electronically excited states $N_2(A^3\Sigma_u^+)$ and $N_2(a'^1\Sigma_u^-)$ (see figure 7(a)) through association ionization. Therefore, the radial profiles of the electron density

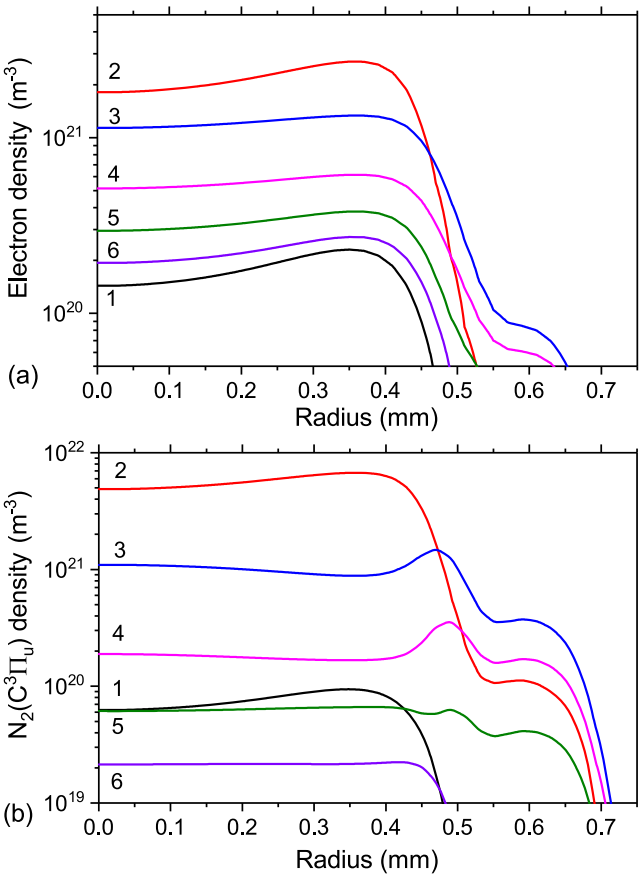

Figure 6. The time evolution of the radial distribution of (a) electron density and (b) the density of $N_2(C^3\Pi_u)$ at the horizontal line $z = 4.1$ cm. Curve 1 corresponds to time 10 ns, 2–20 ns, 3–40 ns, 4–60 ns, 5–100 ns, 6–200 ns. Calculation is performed with full kinetics scheme listed in table 2 and the photoionization considered.

copies the radial distribution of $N_2(A^3\Sigma_u^+)$ and $N_2(a'^1\Sigma_u^-)$ in the afterglow.

Different from the electron density, the radial distribution of $N_2(C^3\Pi_u)$ changes with time significantly. The time evolution of $N_2(C^3\Pi_u)$ density can be analyzed through the following equation:

$$\frac{\mathrm{d}[\mathrm{N_2}(C^3\Pi_u)]}{\mathrm{d}t} = \begin{array}{l} k_\mathrm{exc}(\varepsilon_\mathrm{m})n_\mathrm{e}[\mathrm{N_2}] + k_\mathrm{po}[\mathrm{N_2^*}][\mathrm{N_2^{**}}] - [\mathrm{N_2}(C^3\Pi_u)]/\tau_0 \\ -\sum_j k_q^j[\mathrm{N_2}(C^3\Pi_u)][M_j] - k_\mathrm{qe}n_\mathrm{e}[\mathrm{N_2}(C^3\Pi_u)], \end{array} \quad (16)$$

where $k_\mathrm{exc}(\varepsilon_\mathrm{m})$ is the rate constant of the excitation of grounded N_2 by electron impact, k_po, $[\mathrm{N_2^*}]$ and $[\mathrm{N_2^{**}}]$ are the rate constant of pooling reactions and the density of involved excited states $N_2(A^3\Sigma_u^+, v \leqslant 2)$ and $N_2(A^3\Sigma_u^+, v > 2)$ respectively, τ_0 is the lifetime, k_q^j and $[M_\mathrm{j}]$ are the rate constants of quenching reactions and the density of neutral species as quenchers respectively, and k_qe is the rate constant of $N_2(C^3\Pi_u)$ quenching by electrons.

During the FIW propagation stage, the radial profiles of $N_2(C^3\Pi_u)$ repeats the radial distribution of the electron density due to the dominating electron impact excitation, $\mathrm{d}[\mathrm{N_2}(C^3\Pi_u)]/\mathrm{d}t \propto n_\mathrm{e}$. At the end of the pulse and in the early afterglow ($40 < t < 60$ ns), the maximum of $N_2(C^3\Pi_u)$ density shifts to the periphery of the tube cross section at

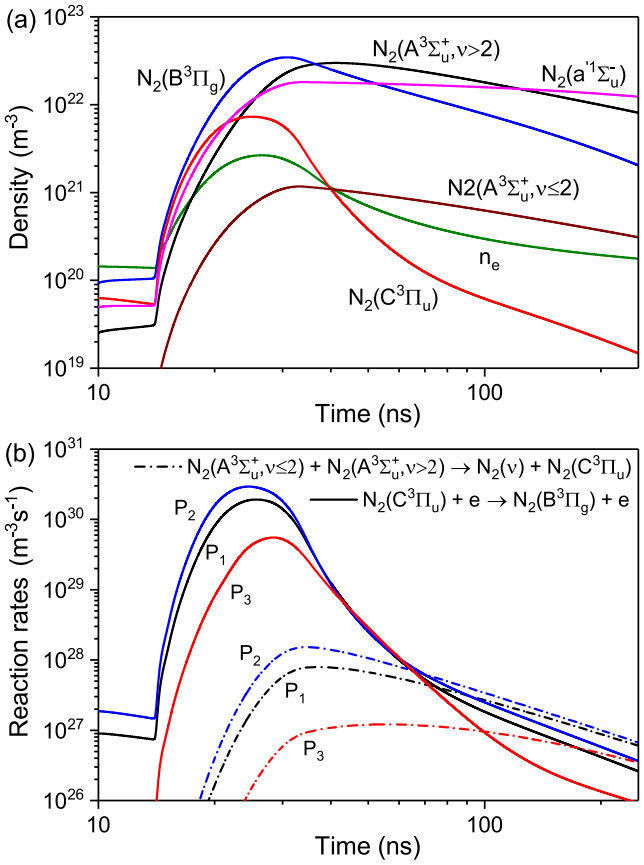

Figure 7. (a) Temporal profiles of six species (e, $N_2(A^3\Sigma_u^+, \upsilon \leqslant 2)$, $N_2(A^3\Sigma_u^+, \upsilon > 2)$, $N_2(B^3\Pi_g)$, $N_2(a'^1\Sigma_u^-)$ and $N_2(C^3\Pi_u)$) involved with the population/depopulation of electrons and $N_2(C^3\Pi_u)$ at the position $r = 0$, $z = 4.1$ cm. (b) The reaction rates of pooling reaction of $N_2(A^3\Sigma_u^+, \upsilon \leqslant 2)$ with $N_2(A^3\Sigma_u^+, \upsilon > 2)$ and the quenching of $N_2(C^3\Pi_u)$ by electrons at three different radial positions P_1 ($r = 0$), P_2 ($r = 0.4$ mm) and P_3 ($r = 0.47$ mm) at horizontal line $z = 4.1$ cm.

$r \approx 0.5$ mm. When $t = 100$ ns, the trend reversed and the maximum of $N_2(C^3\Pi_u)$ density shifts to $r \approx 0.4$ mm, then the density of $N_2(C^3\Pi_u)$ is sustained at the level of 10^{19} m^{-3}. According to figure 7(a), the rates of reactions accounting for the population/depopulation of $N_2(C^3\Pi_u)$ when $t > 20$ ns can be estimated as:

Population: $k_{\rm exc}(\varepsilon_{\rm m})n_{\rm e}[{\rm N_2}] < 10^{24}$ m^{-3} s$^{-1} \ll k_{\rm po}[{\rm N_2^*}]$ $[{\rm N_2^{**}}] \sim 10^{26} - 10^{28}$ m^{-3} s^{-1}

Depopulation: $[{\rm N_2}(C^3\Pi_{\rm u})]/\tau_0 + \sum_j k_{\rm q}^j[{\rm N_2}(C^3\Pi_u)][M_j] + k_{\rm qe}n_{\rm e}[{\rm N_2}(C^3\Pi_u)] \propto [{\rm N_2}(C^3\Pi_u)] \sim k_{\rm qe}n_{\rm e}[{\rm N_2}(C^3\Pi_u)]$.

Therefore, two processes—the pooling reaction between two electronically excited states $N_2(A^3\Sigma_u^+, \upsilon \leqslant 2)$ and $N_2(A^3\Sigma_u^+, \upsilon > 2)$, and the quenching of $N_2(C^3\Pi_u)$ by electrons—can characterize the population and depopulation process when $t > 20$ ns, respectively.

To provide a deeper insight for the time evolution of the radial distribution of the $N_2(C^3\Pi_u)$ density, the temporal profiles of reaction rates of the pooling reaction between $N_2(A^3\Sigma_u^+, \upsilon \leqslant 2)$ and $N_2(A^3\Sigma_u^+, \upsilon > 2)$ and the quenching of $N_2(C^3\Pi_u)$ by electrons, at three typical radial positions P_1, P_2 and P_3 ($r = 0, 0.4, 0.47$ mm, respectively) at horizontal line $z = 4.1$ cm are presented in figure 7(b). The radial profiles show different trends bounded by $t = 70$ ns.

When $t < 70$ ns, the dominated process is the quenching of $N_2(C^3\Pi_u)$ by electrons, and the reaction rate of the process is maximum at P_2, and is minimum at P_3, therefore the shift of the position of the maximum $N_2(C^3\Pi_u)$ density to the periphery of the tube cross section is a result of intensive quenching by electrons in central regions of the tube. When $t > 70$ ns, the pooling reaction of $N_2(A^3\Sigma_u^+, \upsilon \leqslant 2)$ with $N_2(A^3\Sigma_u^+, \upsilon > 2)$ is the most significant $N_2(C^3\Pi_u)$ population process, the reaction rate of the process is maximum at P_2 and its value is larger than that of the quenching by electrons, while the rate of the pooling reaction is minimum at P_3 and its value exceeds that of the quenching process at 100 ns ($t = 80, 70$ ns for P_1 and P_2 respectively), the pooling reaction remodels the radial distribution of $N_2(C^3\Pi_u)$ density in this time range. In a word, the competition between the pooling reaction and the quenching by electrons determines the radial profiles of $N_2(C^3\Pi_u)$ process.

There is an additional question: why are the radial profiles of electrons during development stage different from that of air FIW discharges [23, 35], where the maximum of electron density is on $r = 0$? The secondary emission and photoemission from the surface, and the non–local photoionization process may be responsible. We have tried adjusting merely the photoemission rate and secondary electron emission coefficient in the *nonPDPsim* air FIW code, however no differences in the radial distribution are seen. Taking that photoionization process is one of the key differences between pure nitrogen and air, we will discuss in detail the role of photoionization in the following section.

4.3. The role of photoionization

Photoionization is critical in providing seed electrons for streamer formation and propagation. In atmospheric pressure air, photoionization could produce an equivalent level of 10^{15} m^{-3} of electron density [57]. In this section, the influence of photoionization on temporal-spatial distribution of electrons and $N_2(C^3\Pi_u)$ is assessed by comparing the results obtained via switching the photoionization model on/off.

To calculate without considering photoionization, we have to firstly determine the equivalent background electron density in nitrogen FIW discharges. An approach has been used in reference [57] to determine the value of equivalent background electron density in gas discharges by comparing the direct electron impact ionization rate and photoionization rate. The approach has been successfully validated for streamer propagation in atmospheric air, both in pin-to-plane discharges and pin-to-pin discharges [57].

The photoionization and direct ionization rates, and the electron density at time moments 6, 9, and 12 ns along the symmetric axis $r = 0$ are plotted in figure 8. The background electron density is on the level of ($(4–6) \times 10^{13}$ m^{-3}). This value corresponds to the simulation [58] of a positive streamer propagation in N_2 with 1 ppm O_2 at 200 mbar, in which the background electron density of 10^{13} m^{-3} (no photoionization)

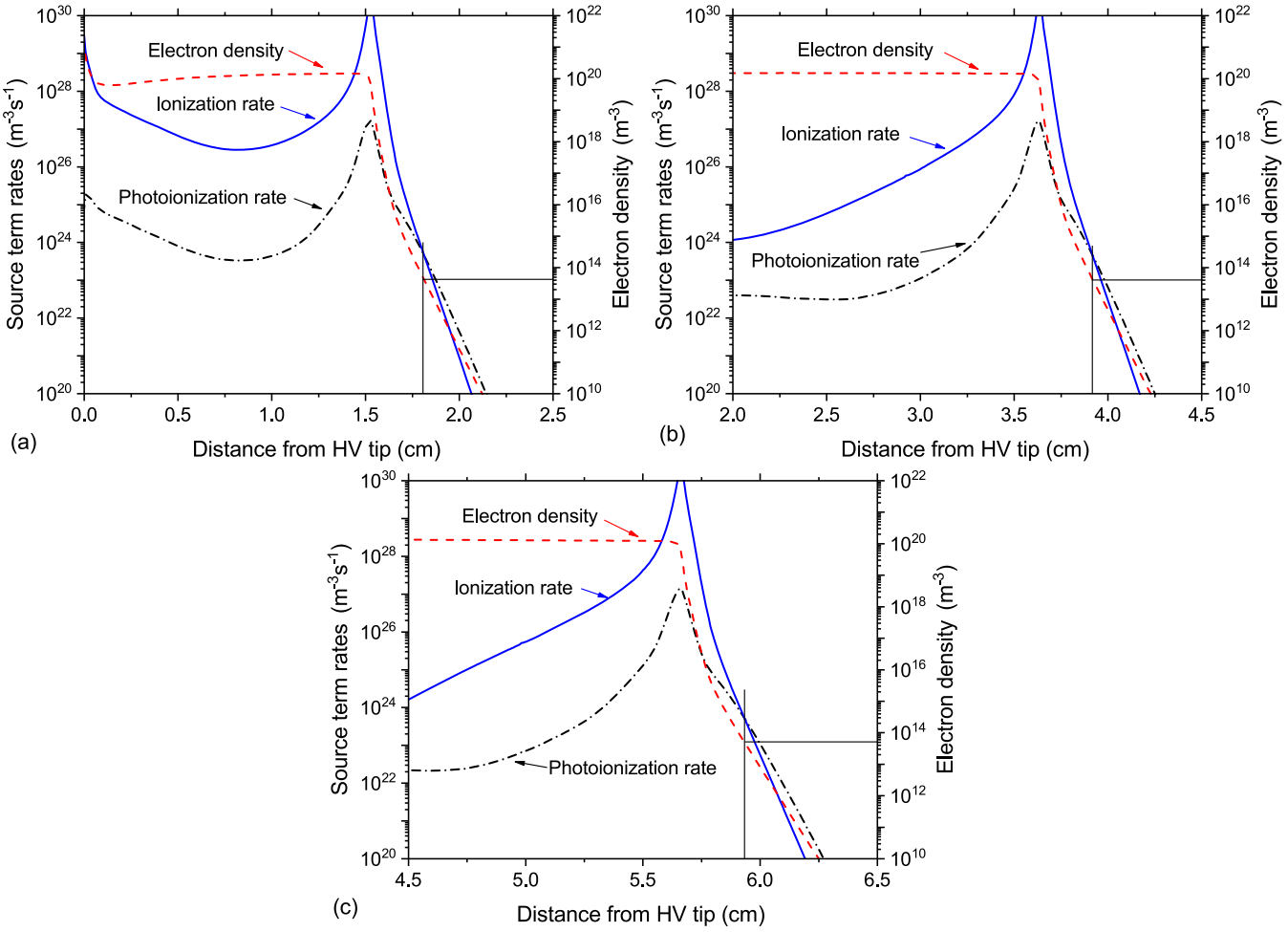

Figure 8. Photoionization and direct ionization rates, and the electron density at time (a) $t = 6$ ns, (b) $t = 9$ ns and (c) $t = 12$ ns along the symmetric axis $r = 0$. The location of equal ionization and photoionization rates, and corresponding electron density are signed by solid lines in figures.

is found to be reasonable in estimating the streamer propagation speed. The background electron density $(1–7) \times 10^{13}$ m^{-3} is used in the following discussions.

The radial distribution of the electron density and $N_2(C^3\Pi_u)$ density calculated with different background electron density n_{e0}, at corresponding time moments 1 ns after the head of ionization waves passing through the probed horizontal line $z = 4.1$ mm, are presented in figure 9.

The streamer channels are thinner when n_{e0} is smaller (according to the radial positions of the maximal electron density), an intuitive explanation can provide physical insight for this difference [59]: considering two points at the same horizontal line $\boldsymbol{r}_1$ (on symmetric axis) and $\boldsymbol{r}_2$ (off symmetric axis), the electron density of two points is initially n_{e0}. At $\boldsymbol{r}_1$ the electric field (or electron energy) is larger, so for the direct ionization rate S we have $S_1 > S_2$. Suppose that $S_2 = (1-\eta)S_1$, n_{ch} is the electron density in the ionized channel, $n_{ch}(\boldsymbol{r}_1) = 2n_{ch}(\boldsymbol{r}_2) = n_{ch}$, then $|\boldsymbol{r}_2 - \boldsymbol{r}_1|$ can be used to estimate the streamer thickness. The electron density n_e as a function as time t can be represented as $n_e = n_{e0}\exp(k_i[N_2]t)$, where k_i is the rate constant of ionization, so $k_i(\boldsymbol{r}_2) = (1-\eta)k_i(\boldsymbol{r}_1)$. By the time that $n_1 = n_{ch}$, we have

$$n_2/n_1 \approx n_2/n_{ch} = \left(\frac{n_{e0}}{n_{ch}}\right)^{\eta}, \tag{17}$$

where we ignored the effect of electron motion for simplicity. In other words, the smaller n_{e0} is, the smaller the ratio n_2/n_1 will be, and with a smaller ratio we expect a thinner streamer. And the smaller preionization level, the larger electron density, which seems contrary to what we expected, in fact this is reasonable, because the smaller streamer thickness means the larger potential gradient (or electric field) in the streamer head and the higher discharge energy density. The radial profiles of $N_2(C^3\Pi_u)$ density show that the value of the $N_2(C^3\Pi_u)$ density with photoionization considered is lowest, because the 'residual' fields behind the FIW heads for the cases without considering photoionization are higher, this is the primary pathway for the population of the electronically excited states [15].

The predefined background electron density of $(1–7) \times 10^{13}$ m^{-3} can be used to approximate the streamer propagation velocity, but cannot always well reproduce the radial distribution in nitrogen FIW. Nevertheless, the calculated preionization level is two orders of magnitude lower than that of air, indicating that in nitrogen the photoionization process is

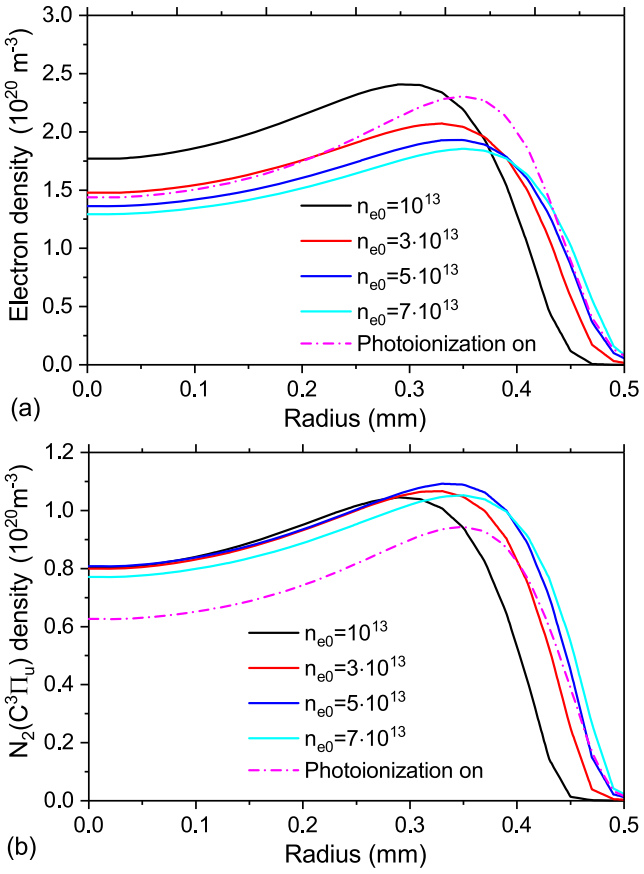

Figure 9. The radial distribution of (a) the electron density and (b) $N_2(C^3\Pi_u)$ density at probed line $z = 4.1$ cm, at corresponding time moments 1 ns after the heads of ionization waves pass through the probed line. Results are obtained via switching the Helmholtz equations on/off.

more local and tends to follow the strong field region, leading to the unique 'hollow' radial profile which is different from that in air [39].

4.4. Energy release and temperature rise

The high SED of FIW is followed by intensive energy release and the FGH process. The spatial-temporal evolution of energy release as well as gas temperature rise are discussed in this section.

Firstly we give the definition of several parameters used in this section. The deposited energy density E_d, total deposited energy E_S, FGH energy density E_{fd}, total FGH energy E_F, SED ω, and heating efficiency η_{FGH} as the functions of time t is written as:

$$E_d(t) = \int_0^t e\boldsymbol{j}_e \cdot \boldsymbol{E}\mathrm{d}t, E_S(t) = \int_\Omega E_d(t)\mathrm{d}\Omega \tag{18}$$

$$E_{fd}(t) = \int_0^t S_{heat}\mathrm{d}t, E_F(t) = \int_\Omega E_{fd}(t)\mathrm{d}\Omega \tag{19}$$

$$\omega(t) = E_d(t)/N(t), \eta_{FGH} = E_{fd}/E_d, \tag{20}$$

where $\boldsymbol{j}_e$ is the electron flux, S_{heat} is the heating power contributed by all exothermic reactions, $N(t)$ is number density of total particles, Ω is the plasma region.

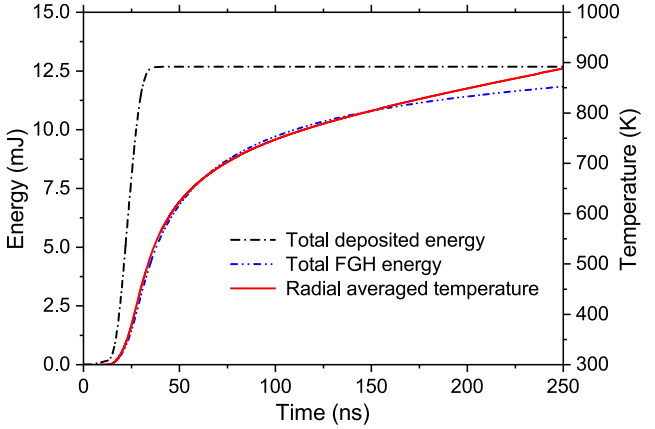

Figure 10. Temporal profiles of the total deposited energy and FGH energy, and the gas temperature averaged over the cross-section of the capillary tube at the horizontal line $z = 4.1$ cm. The curve of FGH energy is multiplied by factor 10.

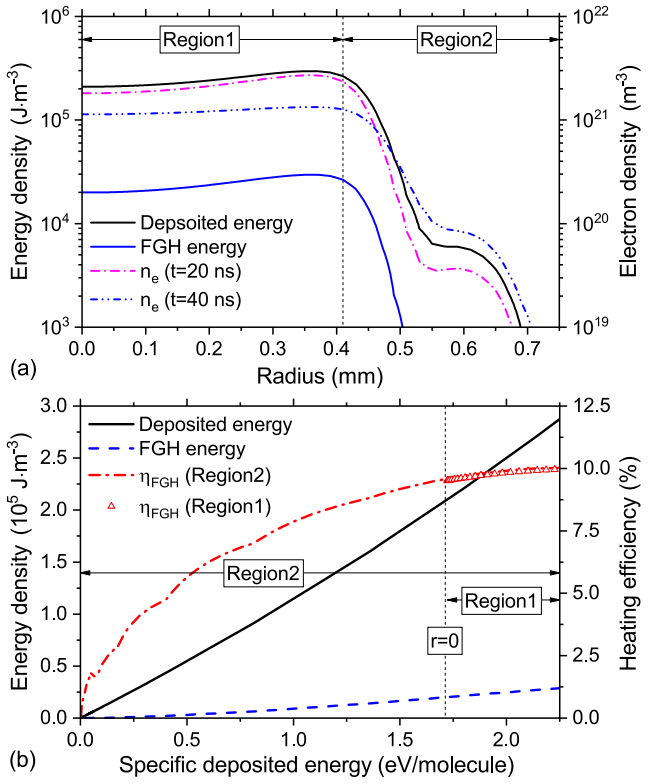

Figure 11. (a) The radial distribution of deposited energy density and FGH energy density, two curves—the electron density at time moments 20 and 40 ns are plotted as references; (b) the deposited energy density, FGH energy density and heating efficiency as the functions of SED. The probed horizontal line is $z = 4.1$ cm. $\omega = 0$, 1.72, 2.25 eV molecule^{-1} corresponding to $r = 0.75$, 0 and 0.41 mm, respectively, and 'region 1' and 'region 2' mean $0 \leqslant r \leqslant 0.41$ and $0.41 \leqslant r \leqslant 0.75$ mm respectively.

The temporal profiles of total deposited energy and FGH energy in the whole capillary tube during the first main pulse are plotted in figure 10. Of the total deposited energy is 12.7 mJ in the pulse stage, about 60% energy is deposited before the time moment of the peak current ($t < 25$ ns). The fraction of

Table 2. Kinetics scheme for FIW in pure nitrogen.

No.	Reaction	Rate constant[a]	Reference
R1	$e + N_2 \rightarrow e + e + N_2^+$	$f(\sigma, \epsilon_m)$	[62]
R2	$e + N_2 \rightarrow e + N_2(A^3\Sigma_u^+, \upsilon \leqslant 2)$	$f(\sigma, \epsilon_m)$	[62]
R3	$e + N_2 \rightarrow e + N_2(A^3\Sigma_u^+, \upsilon > 2)$	$f(\sigma, \epsilon_m)$	[62]
R4	$e + N_2 \rightarrow e + N_2(B^3\Pi_g)$	$f(\sigma, \epsilon_m)$	[62]
R5	$e + N_2 \rightarrow e + N_2(a'^1\Sigma_u^-)$	$f(\sigma, \epsilon_m)$	[62]
R6	$e + N_2 \rightarrow e + N_2(C^3\Pi_u)$	$f(\sigma, \epsilon_m)$	[62]
R7	$e + N_2 \rightarrow e + N(^4S) + N(^2D) + 0.9$ eV [b]	$f(\sigma, \epsilon_m)$	[62]
R8	$e + N_2(B^3\Pi_g) \rightarrow e + N_2(C^3\Pi_u)$	$f(\sigma, \epsilon_m)$	[69]
R9	$e + N(^4S) \rightarrow e + e + N^+$	$f(\sigma, \epsilon_m)$	[70]
R10	$e + N_2^+ \rightarrow N(^4S) + N(^2D) + 3.44$ eV	$1.8 \times 10^{-7}(300/T_e)^{0.39} \times 0.46$	[20]
R11	$e + N_2^+ \rightarrow N(^2D) + N(^2D) + 1.06$ eV	$1.8 \times 10^{-7}(300/T_e)^{0.39} \times 0.46$	[20]
R12	$e + N_2^+ \rightarrow N(^4S) + N(^2P) + 2.25$ eV	$1.8 \times 10^{-7}(300/T_e)^{0.39} \times 0.08$	[20]
R13	$e + N_4^+ \rightarrow N_2 + N_2$	$2 \times 10^{-6}(300/T_e)^{0.5}$	[64]
R14	$e + e + N^+ \rightarrow e + N(^4S)$	$10^{-19}(300/T_e)^{4.5}$	[63]
R15	$e + N^+ + N_2 \rightarrow N(^4S) + N_2$	$6 \times 10^{-27}(300/T_e)^{1.5}$	[63]
R16	$N_2(C^3\Pi_u) \rightarrow N_2(B^3\Pi_g) + \hbar\nu$	2.45×10^7	[65]
R17	$N_2(B^3\Pi_g) \rightarrow N_2(A^3\Sigma_u^+, \upsilon > 2) + \hbar\nu$	2×10^5	[64]
R18	$N_2(A^3\Sigma_u^+, \upsilon > 2) + N(^4S) \rightarrow N_2 + N(^4S) + 6.17$ eV	2×10^{-12}	[65]
R19	$N_2(A^3\Sigma_u^+, \upsilon > 2) + N(^4S) \rightarrow N_2 + N(^2P) + 2.59$ eV	$4 \times 10^{-11}(300/T_{gas})^{0.667}$	[65]
R20	$N_2(A^3\Sigma_u^+, \upsilon \leqslant 2) + N_2(A^3\Sigma_{\{u\}}^+, \upsilon \leqslant 2) \rightarrow N_2(\upsilon) + N_2(B^3\Pi_g) + 3.5$ eV	1.2×10^{-10}	[24]
R21	$N_2(A^3\Sigma_u^+, \upsilon \leqslant 2) + N_2(A^3\Sigma_u^+, \upsilon > 2) \rightarrow N_2(\upsilon) + N_2(B^3\Pi_g) + 3.5$ eV	1.2×10^{-10}	[24]
R22	$N_2(A^3\Sigma_u^+, \upsilon > 2) + N_2(A^3\Sigma_u^+, \upsilon > 2) \rightarrow N_2(\upsilon) + N_2(B^3\Pi_g) + 3.5$ eV	1.2×10^{-10}	[24]
R23	$N_2(A^3\Sigma_{\{u\}}^+, \upsilon \leqslant 2) + N_2(A^3\Sigma_{\{u\}}^+, \upsilon \leqslant 2) \rightarrow N_2(\upsilon) + N_2(C^3\Pi_u) + 0.86$ eV	2.4×10^{-10}	[24]
R24	$N_2(A^3\Sigma_u^+, \upsilon \leqslant 2) + N_2(A^3\Sigma_u^+, \upsilon > 2) \rightarrow N_2(\upsilon) + N_2(C^3\Pi_u) + 0.86$ eV	2.4×10^{-10}	[24]
R25	$N_2(A^3\Sigma_u^+, \upsilon > 2) + N_2(A^3\Sigma_u^+, \upsilon > 2) \rightarrow N_2(\upsilon) + N_2(C^3\Pi_u, \upsilon) + 0.86$ eV	2.4×10^{-10}	[24]
R26	$N_2(B^3\Pi_g) + N_2 \rightarrow N_2(A^3\Sigma_u^+, \upsilon > 2) + N_2(\upsilon)$	10^{-11}	[20]
R27	$N_2(B^3\Pi_g) + N_2(B^3\Pi_g) \rightarrow N_2(B^3\Pi_g, \upsilon) + N_2(\upsilon) + 5$ eV	3.6×10^{-10}	[24]
R28	$N_2(C^3\Pi_u) + N_2 \rightarrow N_2(B^3\Pi_g, \upsilon) + N_2(\upsilon)$	10^{-11}	[20]
R29	$N_2(a'^1\Sigma_u^-) + N_2 \rightarrow N_2(B^3\Pi_g) + N_2(\upsilon)$	2×10^{-13}	[20]
R30	$e + N_2(C^3\Pi_u) \rightarrow e + N_2(B^3\Pi_g)$	10^{-7}	[23]
R31	$e + N_2(B^3\Pi_g) \rightarrow e + N_2(A^3\Sigma_u^+, \upsilon > 2)$	2×10^{-8}	[24]
R32	$N_2(a'^1\Sigma_u^-) + N_2(A^3\Sigma_u^+, \upsilon \leqslant 2) \rightarrow N_4^+ + e$	10^{-11}	[64]
R33	$N_2(a'^1\Sigma_u^-) + N_2(A^3\Sigma_u^+, \upsilon > 2) \rightarrow N_4^+ + e$	10^{-11}	[64]
R34	$N_2(a'^1\Sigma_u^-) + N_2(a'^1\Sigma_u^-) \rightarrow N_4^+ + e$	5×10^{-11}	[64]
R35	$N(^2D) + N_2 \rightarrow N(^4S) + N_2(\upsilon) + 2.35$ eV	$4.52 \times 10^{-14} T_{gas}^{0.68} \exp(-\frac{1438}{T_{gas}})$	[67]
R36	$N(^2P) + N_2 \rightarrow N(^2D) + N_2 + 1.2$ eV	2×10^{-18}	[68]
R37	$N(^2P) + N(^4S) \rightarrow N(^2D) + N(^4S) + 1.2$ eV	1.8×10^{-12}	[68]
R38	$N(^2P) + N_2 \rightarrow N(^4S) + N_2 + 3.58$ eV	$2.89 \times 10^{-18} T_{gas}^{0.5}$	[68]
R39	$N(^2P) + N(^2D) \rightarrow N_2^+ + e$	$3 \times 10^{-16} T_{gas}^{1.2} \exp(\frac{80}{T_{gas}})$	[68]
R40	$N(^2P) + N(^2P) \rightarrow N_2^+ + e$	1.5×10^{-11}	[68]
R41	$N(^4S) + N(^4S) + N_2 \rightarrow N_2(B^3\Pi_g) + N_2 + 2.44$ eV	$8.27 \times 10^{-34} \exp(\frac{500}{T_{gas}})$	[68]
R42	$N_2^+ + N(^4S) \rightarrow N^+ + N_2 + 1.07$ eV	$2.4 \times 10^{-15} T_{gas}$	[63]
R43	$N_4^+ + N_2 \rightarrow N_2^+ + N_2 + N_2$	$2.1 \times 10^{-16} \exp(\frac{T_{gas}}{121})$	[64]
R44	$N_4^+ + N(^4S) \rightarrow N^+ + N_2 + N_2 + 0.013$ eV	10^{-11}	[63]
R45	$N^+ + N(^4S) + N_2 \rightarrow N_2^+ + N_2 + 8.72$ eV	10^{-29}	[63]
R46	$N_2^+ + N_2 + N_2 \rightarrow N_4^+ + N_2 + 1.06$ eV	$6.8 \times 10^{-29}(300/T_{gas})^{1.64}$	[64]

[a]Rate constants are given in s^{-1}, $cm^3\ s^{-1}$ and $cm^6\ s^{-1}$, T_{gas} and T_e are gas temperature and electron temperature (in K), respectively. T_e and T_{gas} are determined by solving electron energy equation and Euler equations, respectively. The energy release in each reaction is from the work of [20, 24, 68].
[b]R7 is a two-step process containing excitation of N_2 by electron impact and the dissociation of the electronic state [20].

deposited energy going to the FGH is 9.4% and 55% FGH energy is generated during the post-discharge stage.

The radial distribution of the deposited energy density and FGH energy density at the horizontal line $z = 4.1$ cm is plotted in figure 11(a). The deposited energy density in the center of the capillary is $E_d \sim 10^5$ J m^{-3}, which is in the same order of magnitude as that of nSDBD [41] at atmospheric pressure, but the much lower gas density at moderate pressure makes the SED increase by tens of times, up to 1.6–2.4 eV molecule^{-1}.

Two additional curves—the profiles of the electron density at time moments 20 ($t = 1/2T_{pulse}$) and 40 ns ($t = T_{pulse}$)—are plotted as references in figure 11(a). The radial profiles of the deposited energy density almost repeats that of the electron density at 20 ns, a simple proportional relationship can be

written as $E_d(r) = K \cdot n_e(r)$, where $K = 10^{-16}$ J is the scale factor. In section 4.2 we have revealed that the radial distribution of the electron density changes slowly both in the pulsed stage and post-discharge stage, thus the electron density can be used to estimate the spatial distribution of deposited energy density, as well as the FGH energy density.

The above analysis indicates a relationship among the deposited energy density E_d, FGH energy density E_{fd} and electron density n_e. To have a deeper understanding, the radial values of E_d, E_{fd} and heating efficiency η_{FGH} are plotted as the functions of SED ω in figure 11(b). Despite ω varies with the radial positions, E_d, E_{fd} and η_{FGH} are all monotonically increasing functions of ω. E_d is a linear function of ω (see equation (20)).

Paper [24] proposed that η_{FGH} is a function of the reduced electric field E/N and ω, this can be confirmed from the curve of η_{FGH} in figure 11(b): the overlapping part of the SED region ($1.72 \leqslant \omega \leqslant 2.25$ eV molecule^{-1}), both in 'region 1' and 'region 2', η_{FGH} equals in this energy interval despite the variation of E/N at different radial positions, indicating that:

(a) η_{FGH} is determined by ω in 'region 1'.
(b) η_{FGH} is determined by both E/N and ω in 'region 2'.
(c) η_{FGH} is only determined by ω when ω is high enough (e.g. $\omega > 1.72$ eV molecule^{-1} in this work).

References [20, 24, 60] analyzed the FGH of nanosecond discharges in nitrogen plasma in the range of the reduced electric fields from 50 to 1000 Td classified the main processes: (i) dissociation of molecules by electron impact; (ii) electron–ion recombination; (iii) pooling reaction of electronically excited states $N_2(A^3\Sigma_u^+)$ and $N_2(B^3\Pi_g)$; (iv) quenching of $N(^2P,^2D)$ atoms by N_2 molecules; (v) charge exchange reactions. Above exothermic processes are considered (see table 2 for details) in the calculation and their fractional contribution in space and time are analyzed in this section.

The fraction of individual reaction k contributing to FGH is defined as follows:

$$\eta_k = \frac{\alpha_k}{\sum_k \alpha_k}, \alpha_k = \int_0^{T_{end}} S_k(t)\mathrm{d}t, \tag{21}$$

where S_k is the heating power of kth reaction. The main processes responsible for FGH in FIW nitrogen discharge can be summarized as:

$$e + N_2 \rightarrow e + N(^4S) + N(^2D) + 0.9 \text{ eV} \tag{22}$$

$$e + N_2^+ \rightarrow N(^4S, ^2D) + N(^4S, ^2D, ^2P) + 2.25 \text{ eV} \tag{23}$$

$$N_2(A^3\Sigma_u^+) + N_2(A^3\Sigma_u^+) \rightarrow N_2(B^3\Pi_g, C^3\Pi_u) + N_2(\upsilon) + 1.74 \text{ eV} \tag{24}$$

$$N_2(B^3\Pi_g) + N_2(B^3\Pi_g) \rightarrow N_2(B^3\Pi_g, \upsilon) + N_2(\upsilon) + 5 \text{ eV} \tag{25}$$

$$N(^2D) + N_2 \rightarrow N(^4S) + N_2(\upsilon) + 2.35 \text{ eV}. \tag{26}$$

The reactions listed above are in correlation with [20, 24, 60]. Detailed contribution from main reactions responsible for FGH at horizontal line $z = 4.1$ cm is plotted in figure 12(a), together with FGH energy density. The radial profiles of the fraction of energy of each reaction extend wider than that of FGH energy density. The spatial distribution of the contribution from each reaction show absolutely different features.

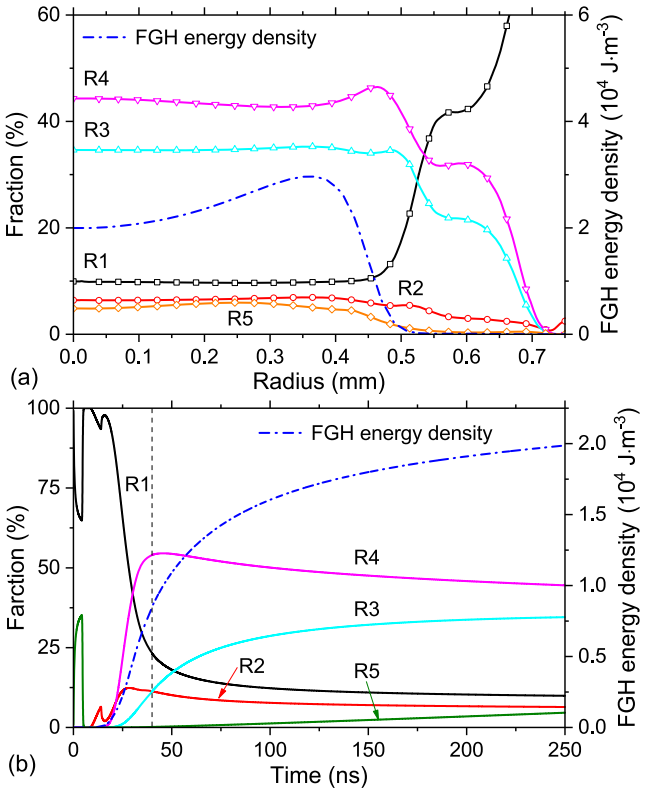

Figure 12. (a) The radial profiles of fractional contribution of main reactions to FGH at horizontal line $z = 4.1$ cm. (b) Temporal profiles of fractional contribution of main reactions to FGH at the probed position $r = 0$, $z = 4.1$ cm, the dash line is $T_{pulse} = 40$ ns. The profiles of FGH energy density are plotted as reference in two sub-figures. R1–R5 represent the reaction (22)–(26).

In central region $r < 0.45$ mm, ω is higher and E/N is lower compared to the peripheral region, the electron density and the density of electronically excited states of molecules/atoms are high, two pooling reactions contribute up to 80% of the energy release, dissociation of N_2 molecules contributes about 10%, and e-N_2^+ recombination and quenching of $N(^2D)$ atoms by N_2 molecules contribute the rest ($\approx$10%).

In the peripheral region, the dissociation of N_2 becomes the dominating process resulting from high E/N and low ω. For example, $E/N = 20\,000$ Td, the rate constant of the dissociation of N_2 is 7×10^{-14} m^3 s^{-1}, while the rate constants of excitation of N_2 to states $N_2(A^3\Sigma_u^+)$ and $N_2(B^3\Pi_u)$ range from 10^{-15} to 3×10^{-15} m^3 s^{-1}, the population of $N_2(A^3\Sigma_u^+)$ and $N_2(B^3\Pi_u)$ is slower than $N(^2D)$, providing the relatively low reactants concentration for two pooling reactions. High E/N also suppresses the e-N_2^+ recombination as rate constants of the e–ion recombination depend negatively on electron temperature. Despite higher population rate of $N(^2D)$ compared to $N_2(A^3\Sigma_u^+)$ and $N_2(B^3\Pi_u)$, the rate of quenching of $N(^2D)$ by N_2 is still small because its rate constant positively depends on ω.

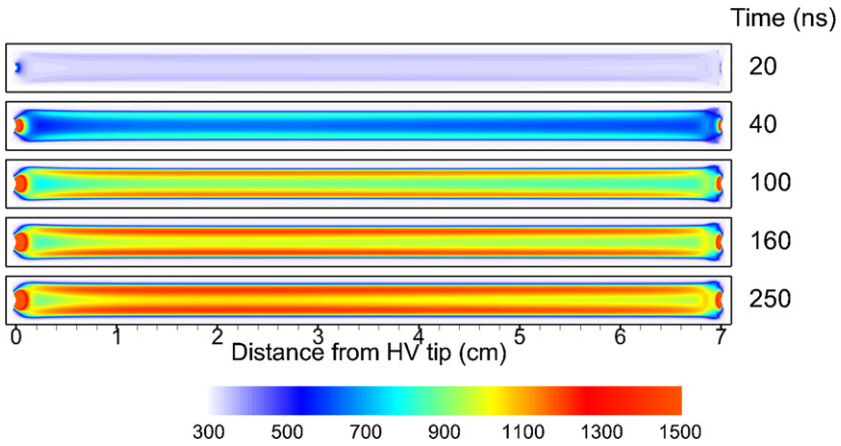

Figure 13. The evolution of the calculated temperature distribution (in K) from 20 to 250 ns.

The fractional contribution from each reaction also varies in time due to the variations of E/N and ω. The fractional contribution of five dominating reactions (22)–(26) to FGH as functions of time at $r = 0, z = 4.1$ cm is plotted in figure 12(b), together with the FGH energy density. The dissociation of N_2 molecules by electron impact contributes over 50% of the total FGH energy when $t < 25$ ns, because electron impact is only effective at high E/N, the energy release from this reaction is almost zero in the post discharge stage. The fractional contribution of e-N_2^+ recombination reaches its peak at 25 ns and then decreases, because N_2^+ lacks the long-lived pathways like electrons in post discharge stage.

Compared to dissociation and recombination reactions, the pooling reactions of $N_2(A^3\Sigma_u^+)$ and $N_2(B^3\Pi_g)$, and the quenching of $N(^2D)$ are more dependent on ω. The high-density $N_2(A^3\Sigma_u^+)$, $N_2(B^3\Pi_g)$ and $N(^2D)$ are effectively produced in high ω regions during the pulse stage and, what is more, the lifetimes of these high-density species are on the level $\sim$100 ns due to the lack of fast depopulation mechanisms. Therefore, these three reactions are main contributors to FGH in the afterglow, at least 60% energy is released from these three reactions.

Besides above common characteristics of reaction (24)–(26), there are two points to be noted: (i) although the rate constants of two pooling reactions are same, the profiles of their fractional contribution show different trends in the afterglow, because the decay rate of $N_2(B^3\Pi_g)$ is faster than that of $N_2(A^3\Sigma_u^+)$; (ii) only the slope of the fractional contribution of reaction (26) keeps nearly constant in the whole stage, as its rate constant positively depends on gas temperature (see R35 in table 2), the process makes a difference when $T_{\rm gas} > 1500$ K [24].

The direct consequence of FGH is the rise of the gas temperature in the conductive channel. The calculated temperature distribution from 20 to 250 ns is presented in figure 13. 2D maps of the temperature show hollow structures similar with the electron density, deposited energy and FGH energy. The radially averaged gas temperature of the horizontal line $z = 4.1$ cm has been compared with the total deposited energy and FGH energy in figure 10, the temperature rise within 250 ns is 600 K compared to about 450 K in reference [24], the gap is as a result of the overestimation of SED (calculated/experimental current value 65 vs 80 A, section 4.1).

5. Conclusions

In the present work, the FIWs operated in pure nitrogen at 27 mbar is studied numerically with existing measurements. The classical fluid model based on local mean energy approximation and an extended three term Helmholtz photoionization model is proposed and validated.

The development of nitrogen FIW has been discussed. The electron density in the head of ionization wave can reach up to (1–3) $\times$ 10^{20} m^{-3} during its nearly 10 ns propagation stage, with an averaged propagation speed of 0.7 cm ns^{-1}. The electric field E/N in the FIW head exceeds 10 000 Td, producing an ionization rate above 10^{30} m^{-3} s^{-1}. The distribution of the electron density shows the hollow structure with the higher magnitude off the symmetric axis. A sheath is formed near the dielectric wall, with a thickness of 250 μm and the electron density lower than 10^{19} m^{-3}, about 20 times of the Debye length.

The calculated electric field and current are compared with electrical measurements, quantitative agreements are achieved. The discrepancies between modeling and measurements lie in the inception stage and before gap closing are discussed.

The temporal-spatial evolution of electrons and $N_2(C^3\Pi_u)$ are analyzed. During FIW development, the radial profiles of the $N_2(C^3\Pi_u)$ density repeats the electron density profile, the maximum density appear off axis. In the afterglow, the radial profiles of electron density changes slowly ($n_e \sim 10^{20}$ m^{-3}) and repeats the radial distribution of $N_2(A^3\Sigma_u^+)$ and $N_2(a'^1\Sigma_u^-)$ due to associative ionization; the radial profiles of $N_2(C^3\Pi_u)$ changes significantly in the afterglow, due to competition between the pooling and quenching reactions. The implementation of pooling reaction of $N_2(A^3\Sigma_u^+)$ is critical to correctly model the time evolution and spatial distribution of $N_2(C^3\Pi_u)$.

The role of photoionization on nitrogen FIW is studied. Equivalent background electron density of photoionization for nitrogen FIW discharges is obtained by comparing the source terms of electron impact ionization and photoionization,

ranging from 4×10^{13} to 6×10^{13} m^{-3}, two orders of magnitudes lower than that in air streamers. The influences of photoionization on the radial distribution of electrons and $N_2(C^3\Pi_u)$ in the development stage are analyzed via switching off the photoionization model. The smaller background electron density, the thinner streamer channel becomes.

Energy properties and FGH are analyzed. The total deposited energy is 12.7 mJ in discharge, 9.4% deposited energy is converted to FGH. The heating efficiency η_{FGH} is confirmed to be a function of electric field E/N and SED ω, and its value tends to 10% with increased SED. Main reactions contributing to FGH are summarized, in the central region $r < 0.45$ mm pooling reaction of $N_2(A^3\Sigma_u^+)$ and $N_2(B^3\Pi_g)$ contributes 80% energy release, electron impact dissociation of N_2 molecules contributes 10%, while e-N_2^+ recombination and quenching of $N(^2D)$ atoms by N_2 molecules contribute the rest. The maximal local temperature rise of 1200 K is observed as a consequence of FGH in 250 ns.

Modeling FIWs initialized by nanosecond pulses at moderate pressures is challenging work for a fluid code, i.e. the high energy deposition leads to strong dissociation that may even change the EEDF, the inception 'shoulder' is still unsolved in the framework of fluid model, and runaway electrons have to be considered when modeling a negative FIW. The classical fluid model has to be extended in the future for more extreme conditions.

Acknowledgments

The work was partially supported by the National Natural Science Foundation of China (No. 52025064, 51907204, 51790511, 91941105, 91941301), and Fund of State Key Laboratory of IPOC (BUPT) (No. IPOC2019ZZ04). The authors are thankful to Professor Svetlana Starikovskaia in Ecole Polytechnique and the young research group in Atelier des Plasmas for fruitful discussions.

Data availability statement

The data that support the findings of this study are available upon reasonable request from the authors.

Appendix A. Kinetics scheme

The kinetics scheme used for nitrogen FIW modeling is based on recognized investigations on chemical kinetics of nitrogen/air plasma, and on the cycle of works on optical actinometry of nCD [18, 30, 39, 61], the scheme is combined with the following parts: (i) ionization and excitation of grounded N_2 and N-atom by direct electron impact, optical radiation reactions, as well as ion conversion reactions, mainly coming from classical schemes [62–65] which have been intensively used in air/nitrogen plasma modeling; (ii) associative ionization reactions involved with $N_2(a'^1\Sigma_u^-)$ and $N_2(A^3\Sigma_u^+)$ [64, 66], coming from kinetics studies on low-pressure nitrogen discharges and post-discharges; (iii) quenching of $N_2(C^3\Pi_u)$ [23] and $N_2(B^3\Pi_g)$ [24] by electrons, proposed in recent years to correctly model the evolution of these two species at high SED; and (iv) quenching of excited states of molecular nitrogen or N-atom accounting for the FGH [20, 24, 67, 68].

The following neutral, charged, excited species are taken into account: e, N_2, N_2^+, N_4^+, N^+, $N_2(A^3\Sigma_u^+, \upsilon \leqslant 2)$, $N_2(A^3\Sigma_u^+, \upsilon > 2)$, $N_2(B^3\Pi_g)$, $N_2(a'^1\Sigma_u^-)$, $N_2(C^3\Pi_u)$, $N(^4S)$, $N(^2D)$ and $N(^2P)$. The scheme includes 13 species and 46 reactions, detailed reactions and corresponding rates are given in table 2. N_3^+ is excluded in the scheme for two reasons: (i) N_3^+ mainly populates via ion conversion processes, such processes has tiny impact on our interests in FIW (e.g. propagation pattern, electron density, $N_2(C^3\Pi_u)$, FGH); (ii) to the authors' best knowledge, no literature has demonstrated the significance of N_3^+, neither in glow discharges nor FIW. The electron–electron collision are taken into account to correctly solve EEDF when ionization degree is relatively high ($n_e/N_{gas} > 2 \times 10^{-3}$) and electric field is low (<100 Td) [23, 24].

The electronically excited state of nitrogen $N_2(A^3\Sigma_u^+)$ is splitted into $N_2(A^3\Sigma_u^+, \upsilon \leqslant 2)$ and $N_2(A^3\Sigma_u^+, \upsilon > 2)$ to correctly model $N_2(C^3\Pi_u)$, similar treatment can be found in [30, 61], where $N_2(A^3\Sigma_u^+)$ is splitting into $N_2(A^3\Sigma_u^+, \upsilon \leqslant 2)$ and $N_2(A^3\Sigma_u^+, \upsilon > 2)$ to correctly model O-atom. The reasonableness and validity of the splitting would be discussed in appendix B. $N_2(B^3\Pi_g)$ is the sum of three states $N_2(B^3\Pi_g)$, $N_2(W^3\Delta_u)$ and $N_2(B'^3\Sigma_u^-)$ to keep consistent with [24], otherwise the FGH energy and gas temperature would be significantly underestimated; keeping the same as [30], $N_2(a'^1\Sigma_u^-)$ is the sum of three states $N_2(a'^1\Sigma_u^-)$, $N_2(a^1\Pi_g)$ and $N_2(W^1\Delta_u)$, $N_2(C^3\Pi_u)$ is the sum of states $N_2(C^3\Pi_u)$ and $N_2(E^3\Sigma_g^+)$.

Recently, TALIF measurements of N-atom in the afterglow of an FIW discharge demonstrated a rather high dissociation degree of 9.7% and N-atom density of 1.29×10^{17} cm^{-3} was obtained at the SED of 1.67 eV $molecule^{-1}$ [22]. The dissociation of electronically excited molecules by electron impact [69], stepwise dissociation of molecular nitrogen was introduced to explain the high dissociation degree:

$$e + N_2(A^3\Sigma_u^+, B^3\Pi_g, C^3\Pi_u) \rightarrow e + N(^4S) + N(^4S, ^2D), k = f(\sigma, \epsilon_m). \quad (27)$$

However, these stepwise dissociation processes are not taken into account in this work. Because reaction (27) was just used to qualitatively explain the possible factors accounting for high dissociation degree, the validation between kinetics modeling and experiments has not been fully completed yet [22].

Appendix B. Analysis of splitting of $N_2(A^3\Sigma_u^+)$ state

We have mentioned in appendix A it is necessary to split the electronically excited state $N_2(A^3\Sigma_u^+)$ into $N_2(A^3\Sigma_u^+, \upsilon \leqslant 2)$ and $N_2(A^3\Sigma_u^+, \upsilon > 2)$ to correctly model $N_2(C^3\Pi_u)$. Here we discuss two problems: why not we just use the pooling reaction of $N_2(A^3\Sigma_u^+, \upsilon \leqslant 2)$ as the source of $N_2(C^3\Pi_u)$ and why we need the split. The decay time of $N_2(C^3\Pi_u)$ in section 4.2 showed good quantitative agreement with optical emission measurements [23], the influence of the implementation of

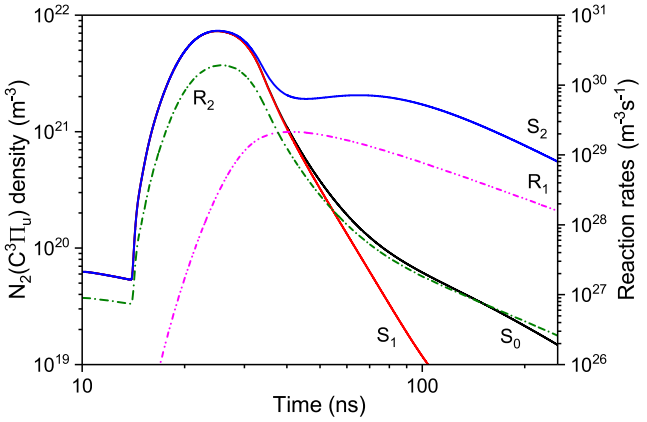

Figure 14. Temporal profiles of $N_2(C^3\Pi_u)$ density under different assumptions about the kinetics model (see text), and the rates of two reactions concerning the production/loss of $N_2(C^3\Pi_u)$: S_0-the density curve obtained with full kinetics scheme in table 2; S_1-the density curve obtained when excluding the pooling reaction of $N_2(A^3\Sigma_u^+, \upsilon \leqslant 2)$ with $N_2(A^3\Sigma_u^+, \upsilon > 2)$ as the source of $N_2(C^3\Pi_u)$ (conservative splitting); S_2-the density curve obtained when including the pooling reaction of $N_2(A^3\Sigma_u^+, \upsilon > 2)$ as the source of $N_2(C^3\Pi_u)$ (no splitting). R_1–the rate of the pooling reaction of $N_2(A^3\Sigma_u^+, \upsilon > 2)$; R_2-the rate of the $N_2(C^3\Pi_u)$ quenching by electrons. The probed position locates at $r = 0$, $z = 4.1$ cm.

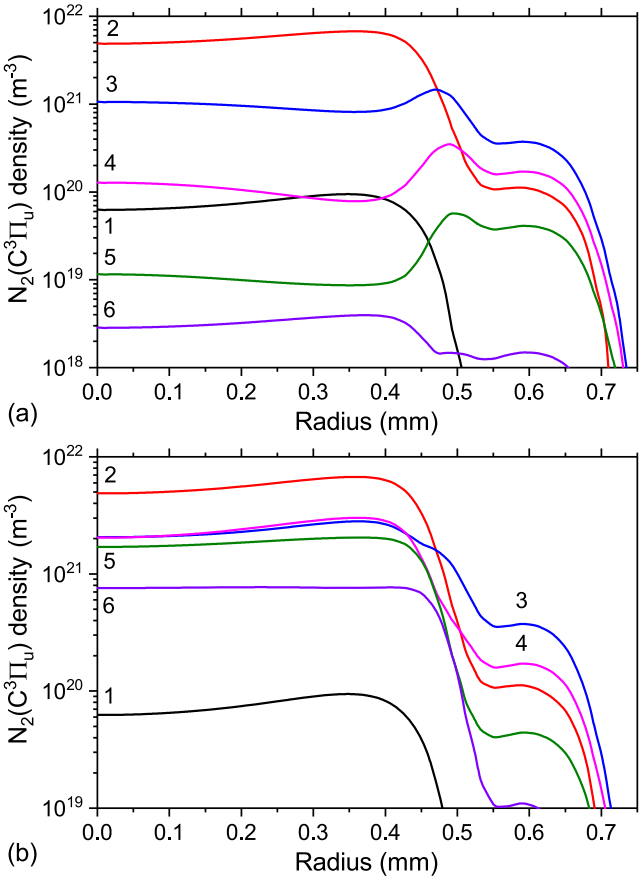

Figure 15. Time evolution of the radial distribution of $N_2(C^3\Pi_u)$ density at the horizontal line $z = 4.1$ cm under different assumptions about the kinetics model (see text): (a) excluding the pooling reaction of $N_2(A^3\Sigma_u^+, \upsilon \leqslant 2)$ with $N_2(A^3\Sigma_u^+, \upsilon > 2)$ as the source of $N_2(C^3\Pi_u)$ (conservative splitting); (b) including the pooling reaction of $N_2(A^3\Sigma_u^+, \upsilon > 2)$ as the source of $N_2(C^3\Pi_u)$ (no splitting). Curve 1 corresponds to time 10 ns, 2–20 ns, 3–40 ns, 4–60 ns, 5–100 ns, 6–200 ns.

kinetics scheme on the temporal-spatial evolution of $N_2(C^3\Pi_u)$ will be discussed below.

Temporal profiles of $N_2(C^3\Pi_u)$ density at the probed position ($r = 0$, $z = 4.1$ cm) under different assumptions about the kinetics model are presented in figure 14. The strategy of the conservative splitting—only including the pooling reaction of $N_2(A^3\Sigma_u^+, \upsilon \leqslant 2)$ as the source of $N_2(C^3\Pi_u)$, underestimates the $N_2(C^3\Pi_u)$ density by nearly one order of magnitude comparing with the results obtained with full kinetics scheme when $t = 100$ ns. Meanwhile no splitting—including the pooling reaction of $N_2(A^3\Sigma_u^+, \upsilon > 2)$ as the source of $N_2(C^3\Pi_u)$significantly overestimates the $N_2(C^3\Pi_u)$ density by more than two orders of magnitude at the end of main pulse. Moreover, a peak of the $N_2(C^3\Pi_u)$ density appears at 70 ns, the time evolution of $N_2(C^3\Pi_u)$ is essentially changed. The above changes resulting from two strategies can be explained by comparing the rates of pooling reaction of $N_2(A^3\Sigma_u^+, \upsilon > 2)$ and that of the quenching of $N_2(C^3\Pi_u)$ by electrons, see figure 14. $N_2(A^3\Sigma_u^+, \upsilon > 2)$ is the long-lived species whose density is in the order of 10^{22} m^{-3} (see figure 7(b)), and this results in rather high rates of the pooling reaction ($> 10^{28}$ m^{-3}), while the rate of the main pathway consuming $N_2(C^3\Pi_u)$—the quenching of $N_2(C^3\Pi_u)$ by electrons—decreases with decaying electron density and is lower than the production rate after $t = 40$ ns.

The time evolution of the radial distribution of the $N_2(C^3\Pi_u)$ density at horizontal line $z = 4.1$ cm under different assumptions about the kinetics model is presented in figure 15. The radial profiles of the $N_2(C^3\Pi_u)$ density are essentially changed for both the strategy of conservative splitting and no splitting, the former obviously magnify the gap between the minimum and the maximum of the $N_2(C^3\Pi_u)$ density in the hollow regions of the capillary, while the latter 'wipe away' the gap and the profiles changes slowly in the afterglow. These substantial changes precisely demonstrate the aforementioned claims on the evolution mechanism of $N_2(C^3\Pi_u)$—the temporal-spatial evolution of $N_2(C^3\Pi_u)$ is dominated by the competition between the pooling reaction of $N_2(A^3\Sigma_u^+, \upsilon \leqslant 2)$ and $N_2(A^3\Sigma_u^+, \upsilon > 2)$ and the quenching by electrons.

ORCID iDs

Xiancong Chen https://orcid.org/0000-0002-9924-7999
Yifei Zhu https://orcid.org/0000-0001-8989-0051
Yun Wu https://orcid.org/0000-0002-8575-0665

References

[1] Leonov S B, Adamovich I V and Soloviev V R 2016 *Plasma Sources Sci. Technol.* **25** 063001
[2] Singh A and Little J 2020 *J. Phys. D: Appl. Phys.* **53** 164004

[3] Komuro A, Takashima K, Suzuki K, Kanno S, Nonomura T, Kaneko T, Ando A and Asai K 2018 *Plasma Sources Sci. Technol.* **27** 104005
[4] Starikovskiy A and Aleksandrov N 2013 *Prog. Energy Combust. Sci.* **39** 61–110
[5] Adamovich I V and Lempert W R 2014 *Plasma Phys. Control. Fusion* **57** 014001
[6] Starikovskaia S M 2014 *J. Phys. D: Appl. Phys.* **47** 353001
[7] Ju Y and Sun W 2015 *Prog. Energy Combust. Sci.* **48** 21–83
[8] Li H-P, Ostrikov K and Sun W 2018 *Phys. Rep.* **770–772** 1–45
[9] Snoeckx R and Bogaerts A 2017 *Chem. Soc. Rev.* **46** 5805–63
[10] Kozák T and Bogaerts A 2014 *Plasma Sources Sci. Technol.* **23** 045004
[11] Lin B, Wu Y, Zhu Y, Song F and Bian D 2019 *Appl. Energy* **235** 1017–26
[12] Lietz A M and Kushner M J 2016 *J. Phys. D: Appl. Phys.* **49** 425204
[13] Soueid M, Dobbelaar M C F, Bentouati S, Bardet S M, O'Connor R P, Bessières D, Paillol J, Leveque P and Arnaud-Cormos D 2018 *Med. Biol. Eng. Comput.* **56** 85–97
[14] Nijdam S, Teunissen J and Ebert U 2020 *Plasma Sources Sci. Technol.* **29** 103001
[15] Starikovskaia S M, Anikin N B, Pancheshnyi S V, Zatsepin D V and Starikovskii A Y 2001 *Plasma Sources Sci. Technol.* **10** 344–55
[16] Anikin N B, Zavialova N A, Starikovskaia S M and Starikovskii A Y 2008 *IEEE Trans. Plasma Sci.* **36** 902–3
[17] Takashima K, Adamovich I V, Xiong Z, Kushner M J, Starikovskaia S, Czarnetzki U and Luggenhölscher D 2011 *Phys. Plasmas* **18** 083505
[18] Klochko A V, Salmon A, Lemainque J, Popov N A, Booth J-P, Xiong Z, Kushner M J and Starikovskaia S M 2014 Experimental and numerical study of fast gas heating and O atom production in a capillary nanosecond discharge *52nd Aerospace Sciences Meeting AIAA SciTech Forum* (National Harbor, Maryland 13–17 January 2014) (American Institute of Aeronautics and Astronautics) pp 1–17
[19] Klochko A V, Lemainque J, Booth J P and Starikovskaia S M 2015 *Plasma Sources Sci. Technol.* **24** 025010
[20] Popov N A 2011 *J. Phys. D: Appl. Phys.* **44** 285201
[21] Popov N A 2016 *Plasma Sources Sci. Technol.* **25** 044003
[22] Chng T L, Lepikhin N D, Orel I S, Popov N A and Starikovskaia S M 2020 *Plasma Sources Sci. Technol.* **29** 035017
[23] Starikovskaia N D, Klochko A V, Popov N A and Starikovskaia S M 2016 *Plasma Sources Sci. Technol.* **25** 045003
[24] Lepikhin N D, Popov N A and Starikovskaia S M 2018 *Plasma Sources Sci. Technol.* **27** 055005
[25] Dogariu A, Goldberg B M, Byrne S O and Miles R B 2017 *Phys. Rev. Appl.* **7** 024024
[26] Goldberg B M, Chng T L, Dogariu A and Miles R B 2018 *Appl. Phys. Lett.* **112** 064102
[27] Adamovich I V, Butterworth T, Orriere T, Pai D Z, Lacoste D A and Cha M S 2020 *J. Phys. D: Appl. Phys.* **53** 145201
[28] Chng T L, Orel I S, Starikovskaia S M and Adamovich I V 2019 *Plasma Sources Sci. Technol.* **28** 045004
[29] Chng T L, Orel I S, Adamovich I V, Popov N A and Starikovskaia S M 2020 N-atom production at high electric fields: E-FISH and TALIF experiments for understanding fast ionization wave kinetics *AIAA Scitech 2020 Forum* (Orlando, FL 6–10 January 2020) (American Institute of Aeronautics and Astronautics) pp 1–11
[30] Zhu Y, Lepikhin N D, Orel I S, Salmon A, Klochko A V and Starikovskaia S M 2018 *Plasma Sources Sci. Technol.* **27** 075020
[31] Rauf S and Kushner M J 1999 *J. Appl. Phys.* **85** 3460–9
[32] Lay B, Moss R S, Rauf S and Kushner M J 2002 *Plasma Sources Sci. Technol.* **12** 8–21
[33] Huang B-D, Takashima K, Zhu X-M and Pu Y-K 2014 *J. Phys. D: Appl. Phys.* **47** 422003
[34] Huang B-D, Carbone E, Takashima K, Zhu X-M, Czarnetzki U and Pu Y-K 2018 *J. Phys. D: Appl. Phys.* **51** 225202
[35] Klochko A V, Starikovskaia S M, Xiong Z and Kushner M J 2014 *J. Phys. D: Appl. Phys.* **47** 365202
[36] Xiong Z, Robert E, Sarron V, Pouvesle J-M and Kushner M J 2012 *J. Phys. D: Appl. Phys.* **45** 275201
[37] Xiong Z and Kushner M J 2012 *Plasma Sources Sci. Technol.* **21** 034001
[38] Xiong Z, Robert E, Sarron V, Pouvesle J-M and Kushner M J 2013 *J. Phys. D: Appl. Phys.* **46** 155203
[39] Zhu Y, Starikovskaia S M, Babaeva N Y and Kushner M J 2020 *Plasma Sources Sci. Technol.* **29** 125006
[40] Zhu Y, Shcherbanev S, Baron B and Starikovskaia S 2017 *Plasma Sources Sci. Technol.* **26** 125004
[41] Zhu Y and Starikovskaia S 2018 *Plasma Sources Sci. Technol.* **27** 124007
[42] Zhu Y, Wu Y, Wei B, Liang H, Jia M, Song H, Haojun X and Li Y 2019 *J. Phys. D: Appl. Phys.* **53** 145205
[43] Zhu Y and Wu Y 2020 *New J. Phys.* **22** 103060
[44] Kulikovsky A A 1998 *Phys. Rev.* E **57** 7066
[45] Chen X, Zhu Y and Wu Y 2020 *Plasma Sources Sci. Technol.* **29** 095006
[46] Bourdon A, Pasko V P, Liu N Y, Célestin S, Ségur P and Marode E 2007 *Plasma Sources Sci. Technol.* **16** 656–78
[47] Luque A, Ebert U, Montijn C and Hundsdorfer W 2007 *Appl. Phys. Lett.* **90** 081501
[48] Hagelaar G J M and Pitchford L C 2005 *Plasma Sources Sci. Technol.* **14** 722–33
[49] Viehland L A and Mason E A 1995 *At. Data Nucl. Data Tables* **60** 37–95
[50] Zheleznyak M B, Mnatsakanian A K and Sizykh S V 1982 *High Temp. Sci.* **20** 423–8
[51] Pancheshnyi S 2014 *Plasma Sources Sci. Technol.* **24** 015023
[52] Pancheshnyi S V, Starikovskaia S M and Starikovskii A Y 2000 *J. Phys. D: Appl. Phys.* **34** 105–15
[53] Bruggeman P J, Iza F and Brandenburg R 2017 *Plasma Sources Sci. Technol.* **26** 123002
[54] Jánský J, Tholin F, Bonaventura Z and Bourdon A 2010 *J. Phys. D: Appl. Phys.* **43** 395201
[55] Viegas P 2018 Electric field characterization of atmospheric pressure helium plasma jets through numerical simulations and comparisons with experiments *PhD Thesis* Ecole Polytechnique
[56] Chng T L, Brisset A, Jeanney P, Starikovskaia S M, Adamovich I V and Tardiveau P 2019 *Plasma Sources Sci. Technol.* **28** 09LT02
[57] Bourdon A, Bonaventura Z and Celestin S 2010 *Plasma Sources Sci. Technol.* **19** 034012
[58] Wormeester G, Pancheshnyi S, Luque A, Nijdam S and Ebert U 2010 *J. Phys. D: Appl. Phys.* **43** 505201
[59] Nijdam S, Takahashi E, Teunissen J and Ebert U 2014 *New J. Phys.* **16** 103038
[60] Shkurenkov I and Adamovich I V 2016 *Plasma Sources Sci. Technol.* **25** 015021
[61] Klochko A 2014 Excited species chemistry in homogeneous nanosecond discharges with high specific energy deposition *PhD Thesis* Ecole Polytechnique pp 96–8
[62] Phelps A V and Pitchford L C 1985 *Phys. Rev.* A **31** 2932
[63] Kossyi I A, Kostinsky A Y, Matveyev A A and Silakov V P 1992 *Plasma Sources Sci. Technol.* **1** 207–20
[64] Guerra V and Loureiro J 1997 *Plasma Sources Sci. Technol.* **6** 361–72

[65] Capitelli M, Ferreira C M, Gordiets B F and Osipov A I 2001 *Plasma Kinetics in Atmospheric Gases* vol 31 (Berlin: Springer)
[66] Guerra V, Sá P A and Loureiro J 2004 *Eur. Phys. J. Appl. Phys.* **28** 125–52
[67] Galvão B R L, Varandas A J C, Braga J P and Belchior J C 2013 *J. Phys. Chem. Lett.* **4** 2292–7
[68] Volynets A V, Lopaev D V, Rakhimova T V, Chukalovsky A A, Mankelevich Y A, Popov N A, Zotovich A I and Rakhimov A T 2018 *J. Phys. D: Appl. Phys.* **51** 364002
[69] Bacri J and Medani A 1982 *Phys. B+C* **112** 101–18
[70] Wang Y, Zatsarinny O and Bartschat K 2014 *Phys. Rev.* A **89** 062714